Supporting Information

Poly-Pnictogen Bonding: Trapping Halide Ions by a tetradentate Antimony(III) Lewis Acid

J. Louis Beckmann, Jonas Krieft, Yury V. Vishnevskiy, Beate Neumann, Hans-Georg Stammler, and Norbert W. Mitzel*

*Corresponding Author.

Chair of Inorganic and Structural Chemistry, Center for Molecular Materials CM_2
Faculty of Chemistry, Bielefeld University
Universitätsstrasse 25, 33615 Bielefeld (Germany)
E-mail: mitzel@uni-bielefeld.de

Table of Contents

Experimental Procedures

General considerations

All reactions (except aqueous workup) were performed in the absence of water and air using conventional Schlenk techniques with nitrogen as inert gas or in a glove box with argon as inert gas. Volatile compounds were handled using standard high-vacuum techniques. *n*-Pentane and diethyl ether were dried over lithium aluminum hydride and dichloromethane and chloroform were dried over calcium hydride or molecular sieve. Benzene was dried over Na/K alloy. All solvents were distilled and degassed prior to use. Chemicals were purchased from commercial sources and were dried prior to use [antimony trichloride (≥99%), 4-bromotoluene (≥99%), hydrogen chloride (99.8%, Linde), tetrabutylammonium iodide (≥98.0%), tetrabutylammonium bromide (≥98.0%), tetramethylammonium chloride (≥97.0%)]. 1,8-Bis[{bis(pentafluoroethyl)stibanyl}ethynyl]anthracene (**1**)[1], the *syn*-dimer of 1,8-bis[(trimethylstannyl)ethynyl]anthracene (**3**)[2] and chlorobis(pentafluoroethyl)stibane (**4**)[1] were prepared according to literature.

NMR spectra were recorded on a Bruker Avance III 300 or Avance III 500 HD spectrometer at ambient temperature. Chemical shifts were referenced to the residual proton or carbon signal of the solvent (CD_2Cl_2: ^{1}H: 5.32 ppm, ^{13}C: 54.0 ppm; THF-d_8: ^{1}H: 3.58 ppm and 1.73 ppm, ^{13}C: 67.6 ppm and 25.4 ppm) or externally (^{19}F: $CFCl_3$). Elemental analyses were carried out using an EURO EA Elemental Analyzer. IR spectroscopic measurements were performed on a Bruker-Alpha-FT-IR spectrometer with a diamond crystal. SC-XRD was performed on a Rigaku Supernova diffractometer using Cu-Kα or Mo-Kα radiation.

Syntheses

Tetrastibanyl compound 2: To a solution of the *syn*-photodimer of 1,8-bis[(trimethylstannyl)ethynyl]anthracene (1.00 g, 0.91 mmol, **3**) in dichloromethane (15 mL) a solution of chlorobis(pentafluoroethyl)stibane (**4**) in toluene (molar ratio 1:1, 2.05 g, 4.21 mmol, 4.6 equivalents) was added at −5 °C. The reaction mixture was stirred for 1 h cooled and for 3 h at ambient temperature. All volatile compounds were removed under reduced pressure, the obtained beige residue was recrystallized from dichloromethane and the *syn*-photo-dimer of 1,8-bis[{bis(pentafluoroethyl)stibanyl}ethynyl]anthracene (1.26 g, 0.67 mmol, 74%) was obtained as colorless, block-like crystals. – ^{1}H NMR (500 MHz, THF-d_8): δ [ppm] = 7.11 (d, $^3J_{H,H}$ = 7.8 Hz, 4H, H2/H7), 7.04 (d, $^3J_{H,H}$ = 7.4 Hz, 4H, H4/H5), 6.88 (t, $^3J_{H,H}$ = 7.6 Hz, 4H, H3/H6), 5.80 (s, 2H, H9), 4.72 (s, 2H, H10). – ^{13}C{^{1}H} NMR (126 MHz, THF-d_8): δ [ppm] = 145.1 (s, C^q), 144.6 (s, C^q), 133.0 (s, C2/C7), 129.7 (s, C4/C5), 127.1 (s, C3/C6), 120.9 (s, C^q), 115.3 (s, *C*≡C-Sb), 87.3 (s, C≡*C*-Sb), 54.0 (s, C10), 49.6 (s, C9). – ^{13}C{^{19}F} NMR (126 MHz, THF-d_8): δ [ppm] = 123.5 (s, CF_3), 120.1 (s, CF_2), 120.1 (s, CF_2). – ^{19}F NMR (471 MHz, THF-d_8): δ [ppm] = −82.4 (s, CF_3), −82.4 (s, CF_3), −107.1/−109.6 (AB-spin system, CF_2, $^2J_{F,F}$ = 299 Hz), −107.1/−109.8 (AB-spin system, CF_2, $^2J_{F,F}$ = 299 Hz). – ^{1}H NMR (300 MHz, CD_2Cl_2): δ [ppm] = 7.16 (d, $^3J_{H,H}$ = 7.8 Hz, 4H, H2/H7), 7.04 (d, $^3J_{H,H}$ = 7.4 Hz, 4H, H4/H5), 6.91 (t, $^3J_{H,H}$ = 7.5 Hz, 4H, H3/H6), 5.73 (s, 2H, H9), 4.63 (s, 2H, H10). – ^{19}F NMR (282 MHz, CD_2Cl_2): δ [ppm] = −82.0 (s, CF_3), −82.1 (s, CF_3), −106.3/−108.7 (AB-spin system, CF_2, $^2J_{F,F}$ = 297 Hz), −106.5/−108.8 (AB-spin system, CF_2, $^2J_{F,F}$ = 297 Hz). – IR ($\tilde{\nu}$/ cm^{-1}): 2962.7 (w, br), 2142.9 (m, br), 1463.3 (w), 1310.3 (st), 1187.7 (st, br), 1085.2 (st, br), 913.5 (st), 800.3 (m), 773.6 (m), 735.0 (st), 666.9 (m), 610.2 (m). – Elemental analysis calcd (%) for $C_{52}H_{16}F_{40}Sb_4$ (M_r = 1887.68): C 33.09, H 0.85; found: C 33.36, H 0.89.

General procedure for the preparation of the halide adducts

The respective halide adducts [**2**·Cl]$^-$[Me_4N]$^+$, [**2**·Br]$^-$[^{n}Bu_4N]$^+$ and [**2**·I]$^-$[^{n}Bu_4N]$^+$ were prepared in quantitative yield by adding equimolar amounts of tetramethylammonium chloride, tetrabutylammonium bromide, or tetrabutylammonium iodide to a solution of the host **2** (40 mg, 21 µmol) in THF-d_8 in a Young NMR tube. Single crystals of the adducts were obtained by mixing an equimolar amount of host system **2** and halide salt in benzene, dissolving the suspension by heating, and then cooling slowly.

Analytical data for [2·Cl]$^-$[Me_4N]$^+$:

^{1}H NMR (500 MHz, THF-d_8): δ [ppm] = 7.04 (d, $^3J_{H,H}$ = 7.7 Hz, 4H, H2/H7), 6.97 (d, $^3J_{H,H}$ = 7.4 Hz, 4H, H4/H5), 6.80 (t, $^3J_{H,H}$ = 7.6 Hz, 4H, H3/H6), 6.22 (s, 2H, H9), 4.65 (s, 2H, H10), 3.05 (s, 12H, CH_3). – ^{13}C{^{1}H} NMR (126 MHz, THF-d_8): δ [ppm] = 146.6 (s, C^q), 145.0 (s, C^q), 131.9 (s, C2/C7), 129.1 (s, C4/C5), 126.5 (s, C3/C6), 121.6 (s, C^q), 113.2 (s, *C*≡C-Sb), 89.0 (s, C≡*C*-Sb), 55.7 (s, CH_3), 54.2 (s, C10), 49.2 (s, C9). – ^{13}C{^{19}F} NMR (126 MHz, THF-d_8): δ [ppm] = 125.9 (s, CF_3), 125.3 (s, CF_3), 121.7 (s, CF_2), 121.4 (s, CF_2). –

^{19}F NMR (471 MHz, THF-d_8): δ [ppm] = −82.2 (s, CF_3), −107.1/−109.9 (AB-spin system, CF_2, $^2J_{F,F}$ = 301 Hz), −108.4/−110.9 (AB-spin system, CF_2, $^2J_{F,F}$ = 305 Hz). – IR ($\tilde{\nu}$/ cm^{-1}): 2940.5 (w, br), 2141.8 (m, br), 1484.3 (m), 1308.9 (st), 1185.2 (st, br), 1084.3 (st, br), 910.8 (st), 800.3 (m), 772.9 (m), 733.7 (st), 608.4 (m), 507.9 (m). – Elemental analysis calcd (%) for $C_{56}H_{28}F_{40}Sb_4NCl\cdot$ 2.5 C_6H_6 (M_r = 2192.56): C 38.89, H 1.98, N 0.64; found: C 38.89, H 2.35, N 0.65.

Analytical data for [2·Br]$^-$[^{n}Bu$_4$N]$^+$:

^{1}H NMR (500 MHz, THF-d_8): δ [ppm] = 7.03 (d, $^3J_{H,H}$ = 7.7 Hz, 4H, H2/H7), 6.96 (d, $^3J_{H,H}$ = 7.4 Hz, 4H, H4/H5), 6.79 (t, $^3J_{H,H}$ = 7.6 Hz, 4H, H3/H6), 6.24 (s, 2H, H9), 4.65 (s, 2H, H10), 3.22 (m, 8H, CH_2), 1.65 (m, 8H, CH_2), 1.38 (m, 8H, CH_2), 0.99 (t, $^3J_{H,H}$ = 7.4 Hz, 12H, CH_3). – ^{13}C{^{1}H} NMR (126 MHz, THF-d_8): δ [ppm] = 146.8 (s, C^q), 145.0 (s, C^q), 131.9 (s, C2/C7), 129.0 (s, C4/C5), 126.4 (s, C3/C6), 121.7 (s, C^q), 113.5 (s, *C*≡C-Sb), 88.6 (s, C≡*C*-Sb), 59.3 (s, CH_2), 54.2 (s, C10), 49.2 (s, C9), 24.5 (s, CH_2), 20.6 (s, CH_2), 13.9 (s, CH_3). – ^{13}C{^{19}F} NMR (126 MHz, THF-d_8): δ [ppm] = 125.7 (m, CF_3), 125.1 (m, CF_3), 121.7 (m, CF_2), 121.5 (m, CF_2). – ^{19}F NMR (471 MHz, THF-d_8): δ [ppm] = −82.2 (s, CF_3), −82.3 (s, CF_3), −106.7/−109.6 (AB-spin system, CF_2, $^2J_{F,F}$ = 301 Hz), −108.1/−110.6 (AB-spin system, CF_2, $^2J_{F,F}$ = 305 Hz). – IR ($\tilde{\nu}$/ cm^{-1}): 2969.0 (w. br), 2145.0 (m, br), 1462.5 (m), 1308.1 (st), 1184.9 (st, br), 1073.2 (st, br), 911.5 (st), 798.3 (m), 770.8 (m), 734.3 (st), 668.7 (m), 608.5 (m). – Elemental analysis calcd (%) for $C_{68}H_{52}F_{40}Sb_4NBr\cdot$ C_6H_6 (M_r = 2288.17): C 38.84, H 2.56, N 0.61; found: C 39.18, H 2.40, N 0.65.

Analytical data for [2·I]$^-$[^{n}Bu$_4$N]$^+$:

^{1}H NMR (500 MHz, THF-d_8): δ [ppm] = 7.05 (d, $^3J_{H,H}$ = 7.7 Hz, 4H, H2/H7), 6.96 (d, $^3J_{H,H}$ = 7.4 Hz, 4H, H4/H5), 6.79 (t, $^3J_{H,H}$ = 7.6 Hz, 4H, H3/H6), 6.19 (s, 2H, H9), 4.65 (s, 2H, H10), 3.22 (m, 8H, CH_2), 1.65 (m, 8H, CH_2), 1.39 (m, 8H, CH_2), 0.99 (t, $^3J_{H,H}$ = 7.4 Hz, 12H, CH_3). – ^{13}C{^{1}H} NMR (126 MHz, THF-d_8): δ [ppm] = 146.5 (s, C^q), 145.0 (s, C^q), 132.3 (s, C2/C7), 129.0 (s, C4/C5), 126.4 (s, C3/C6), 121.7 (s, C^q), 113.5 (s, *C*≡C-Sb), 88.2 (s, C≡*C*-Sb), 59.3 (s, CH_2), 54.3 (s, C10), 49.4 (s, C9), 24.5 (s, CH_2), 20.6 (s, CH_2), 13.9 (s, CH_3). – ^{13}C{^{19}F} NMR (126 MHz, THF-d_8): δ [ppm] = 125.4 (s, CF_3), 124.9 (s, CF_3), 121.6 (s, CF_2), 121.4 (s, CF_2). – ^{19}F NMR (471 MHz, THF-d_8): δ [ppm] = −82.4 (s, CF_3), −82.4 (s, CF_3), −106.5/−109.4 (AB-spin system, CF_2, $^2J_{F,F}$ = 301 Hz), −107.8/−110.4 (AB-spin system, CF_2, $^2J_{F,F}$ = 305 Hz). – IR ($\tilde{\nu}$/ cm^{-1}): 2969.0 (w), 2145.0 (m, br), 1462.4 (m), 1306.1 (st), 1183.5 (st, br), 1070.5 (st, br), 907.8 (st), 797.9 (m), 734.3 (st), 685.9 (m), 668.7 (m). – Elemental analysis calcd (%) for $C_{68}H_{52}F_{40}Sb_4NI\cdot$ C_6H_6 (M_r = 2335.17): C 38.06, H 2.50, N 0.60; found: C 38.34, H 2.37, N 0.77.

Titration experiments

To a solution of host system **2** in THF-d_8 (50 mM), 0.25 equivalents of the halide salts are incrementally added as a solid and allowed to dissolve. The addition was followed up by ^{1}H and ^{19}F NMR spectroscopy. In the case of tetrabutylammonium iodide and -bromide, amounts greater than one equivalent are soluble, whereas tetramethylammonium chloride is insoluble in THF and is precisely dissolved up to one equivalent through complexation by the host **2**.

Competitive reaction experiments

A solution of the bidentate host system **1** (10 mg, 10.6 mmol, 2 eq.) and one equivalent TBAX (X = Br, I) in THF-d_8 are placed in a Young NMR tube and the solution is investigated by means of NMR spectroscopy. After addition of one equivalent of the tetradentate host system **2** (10 mg, 5.3 mmol, 1 eq.), the solution is again investigated by means of NMR spectroscopy, showing a total formation of [**2**·X]$^-$[^{n}Bu$_4$N]$^+$ (X = Br, I) and free host **1**. In the case of TMACl, precisely 1 equivalent of TMACl is dissolved when the salt is mixed with the host system **2**, whereas merely 0.15 equivalents of TMACl are dissolved when mixed with the bidentate system **1**.

NMR spectroscopic data

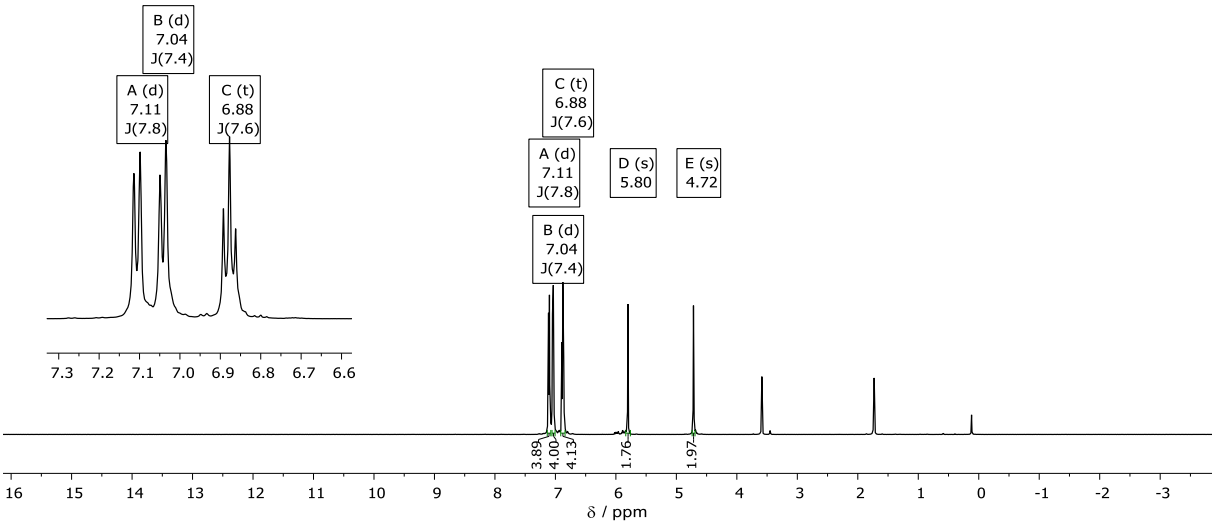

Figure S1. ^{1}H NMR spectrum of tetrastibanyl compound **2** in THF-d_8.

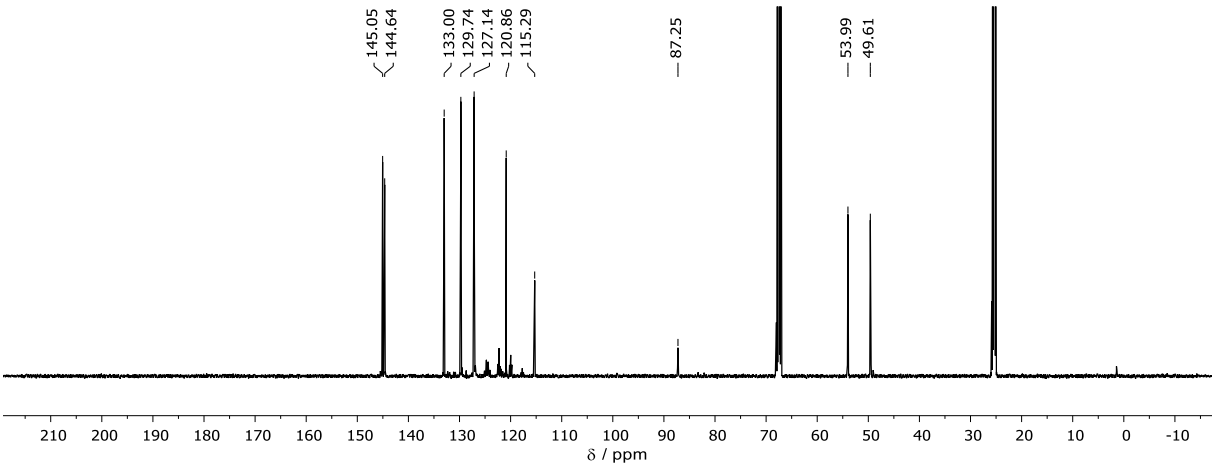

Figure S2. ^{13}C{^{1}H} NMR spectrum of tetrastibanyl compound **2** in THF-d_8.

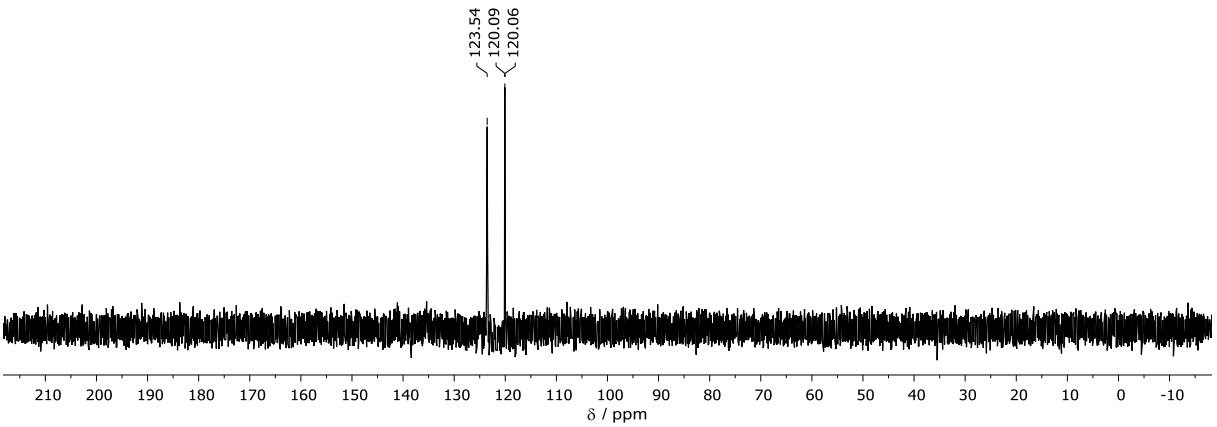

Figure S3. ^{13}C{^{19}F} NMR spectrum of tetrastibanyl compound **2** in THF-d_8.

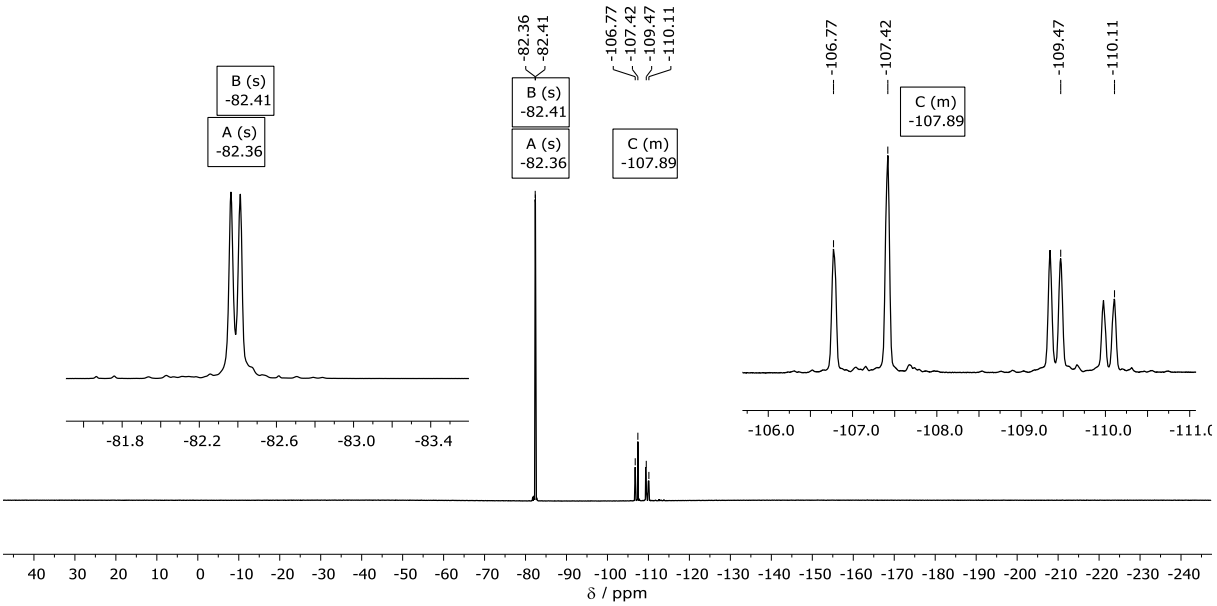

Figure S4. ^{19}F NMR spectrum of tetrastibanyl compound **2** in THF-d_8.

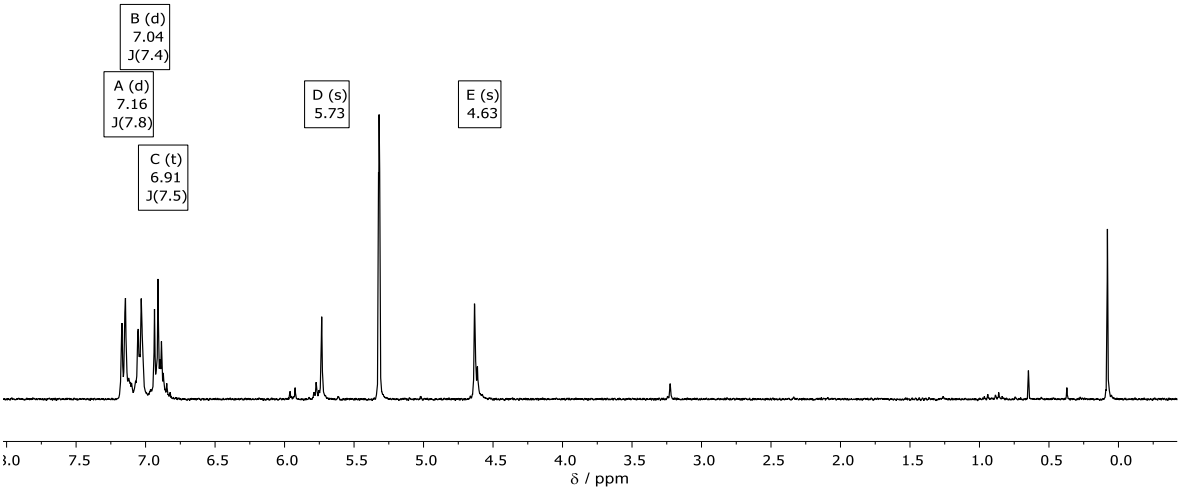

Figure S5. ^{1}H NMR spectrum of tetrastibanyl compound **2** in CD_2Cl_2.

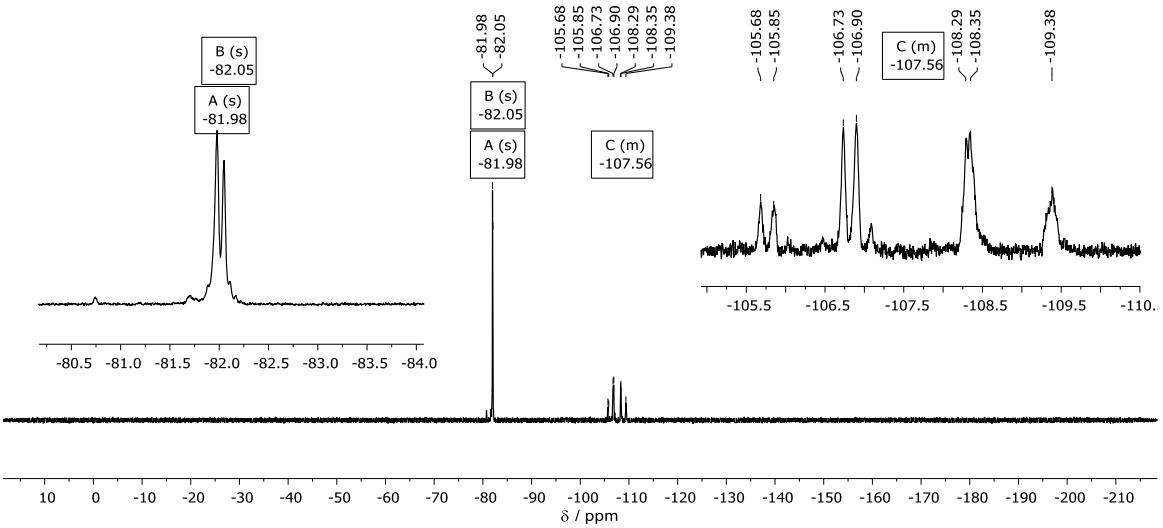

Figure S6. ^{19}F NMR spectrum of tetrastibanyl compound **2** in CD_2Cl_2.

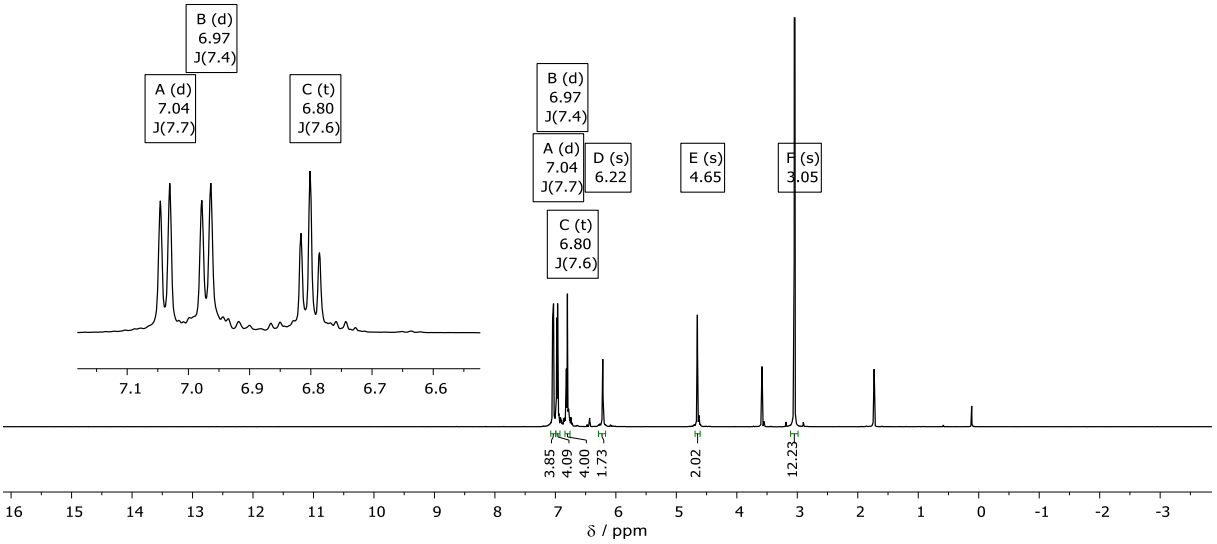

Figure S7. ^{1}H NMR spectrum of [**2**·Cl]$^{-}$[NMe$_4$]$^{+}$ in THF-d_8.

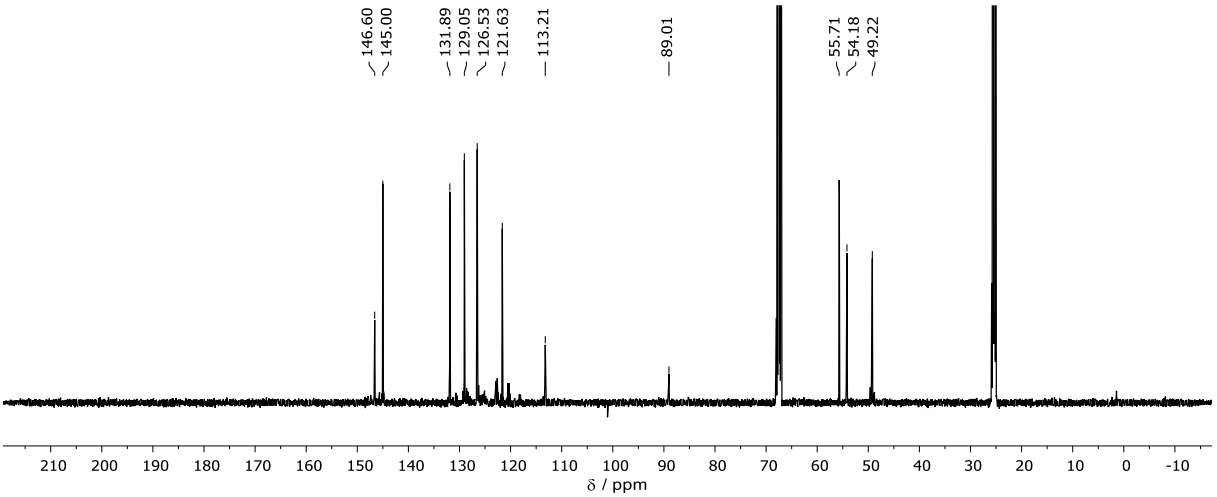

Figure S8. ^{13}C{^{1}H} NMR spectrum of [**2**·Cl]$^{-}$[NMe$_4$]$^{+}$ in THF-d_8.

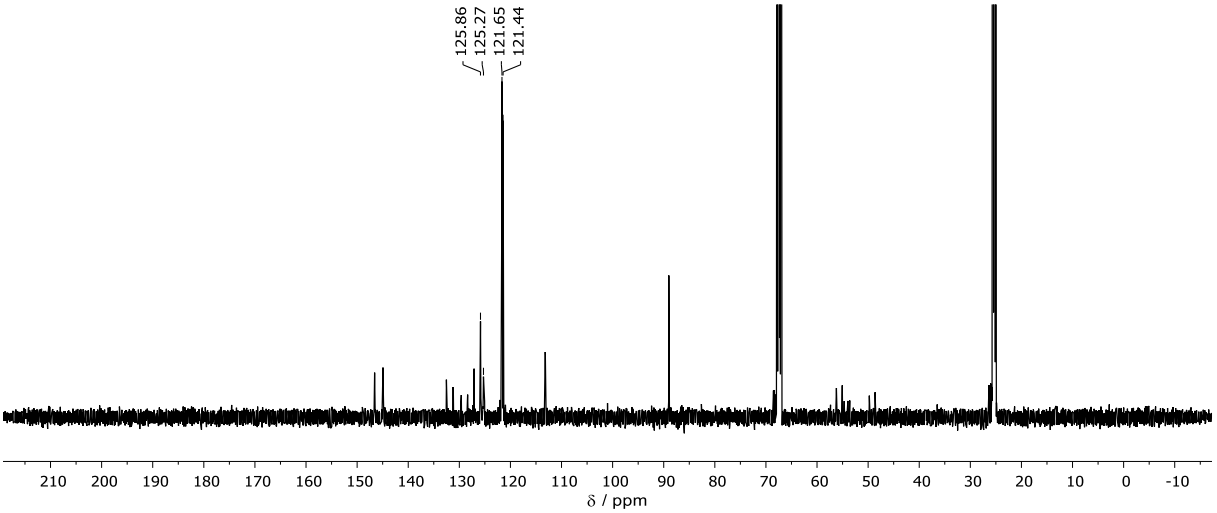

Figure S9. ^{13}C{^{19}F} NMR spectrum of [**2**·Cl]$^{-}$[NMe$_4$]$^{+}$ in THF-d_8.

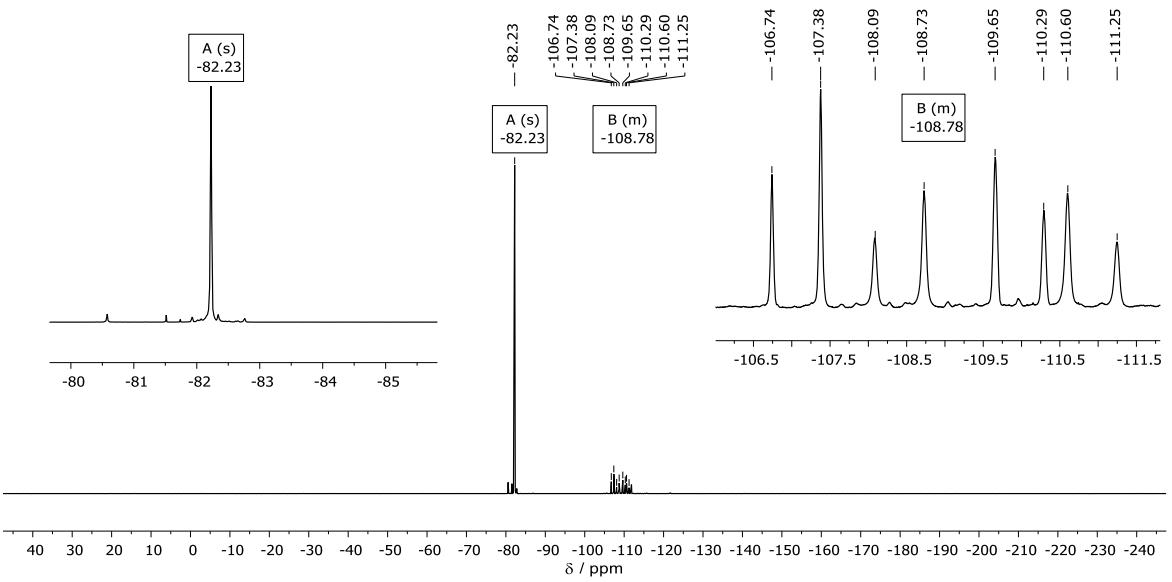

Figure S10. ^{19}F NMR spectrum of [**2**·Cl]$^{-}$[NMe$_4$]$^{+}$ in THF-d_8.

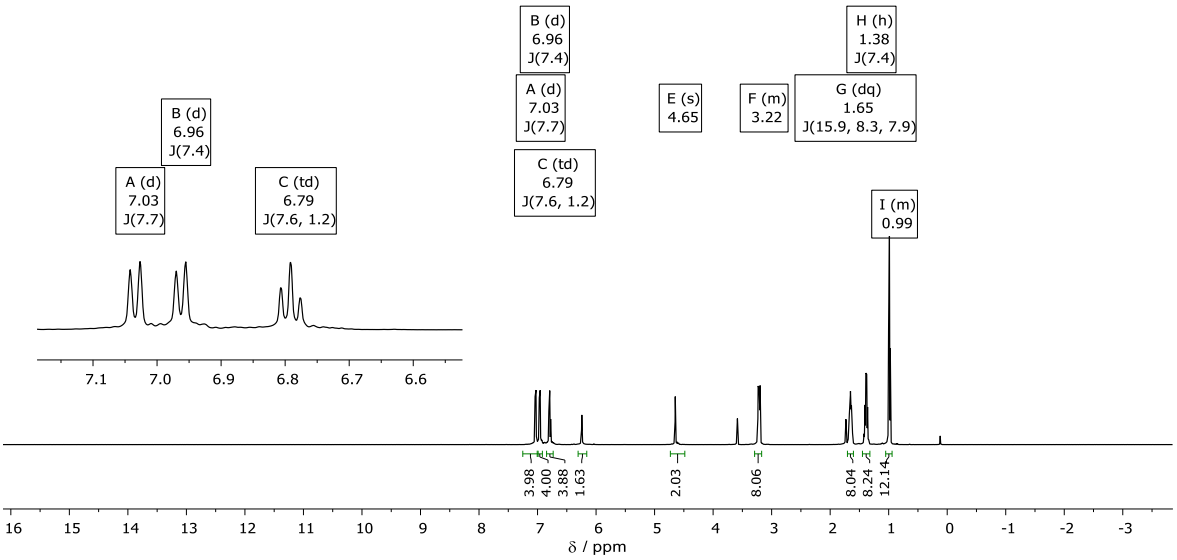

Figure S11. ^{1}H NMR spectrum of [**2**·Br]$^{-}$[N^{n}Bu$_4$]$^{+}$ in THF-d_8.

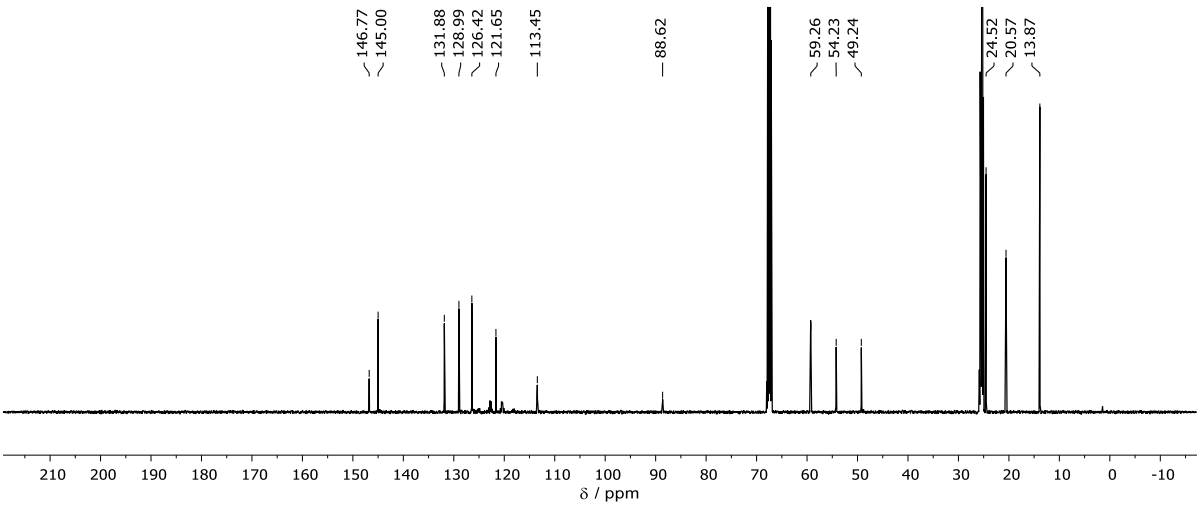

Figure S12. $^{13}C\{^{1}H\}$ NMR spectrum of [**2**·Br]$^{-}$[N^{n}Bu$_4$]$^{+}$ in THF-d_8.

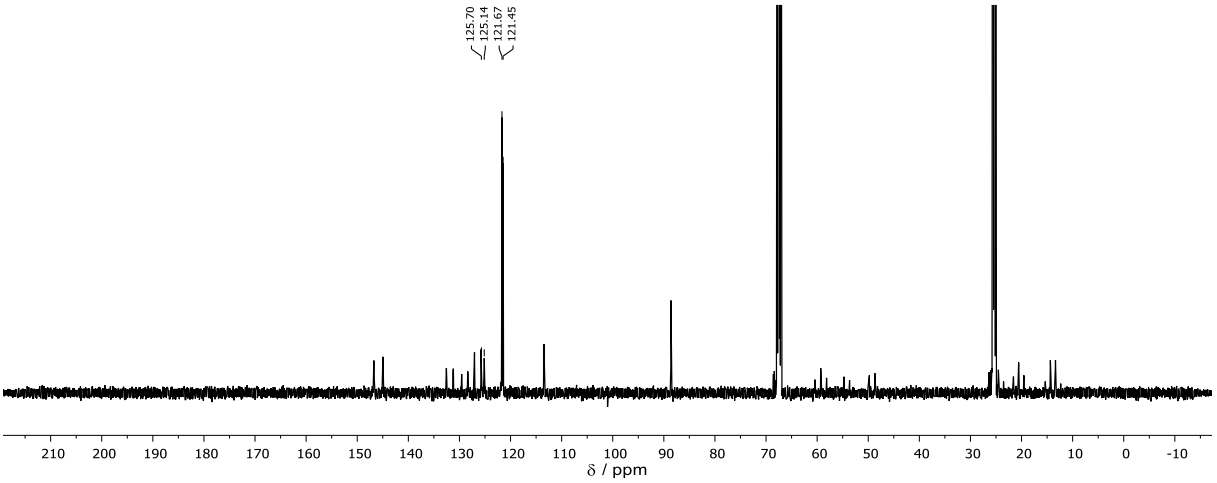

Figure S13. $^{13}C\{^{19}F\}$ NMR spectrum of [**2**·Br]$^-$[N^{n}Bu$_4$]$^+$ in THF-d_8.

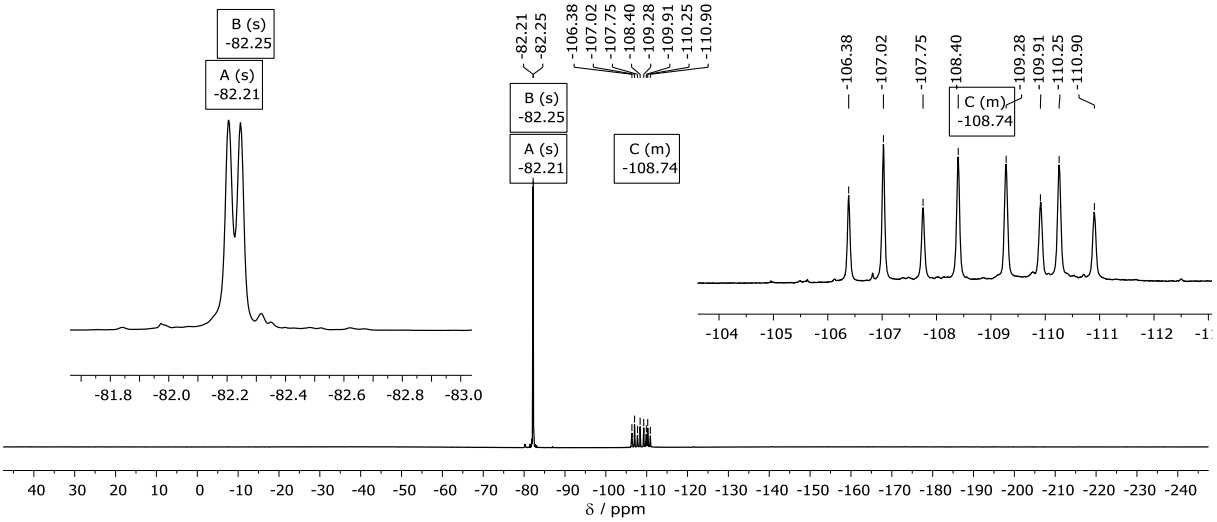

Figure S14. ^{19}F NMR spectrum of [**2**·Br]$^-$[N^{n}Bu$_4$]$^+$ in THF-d_8.

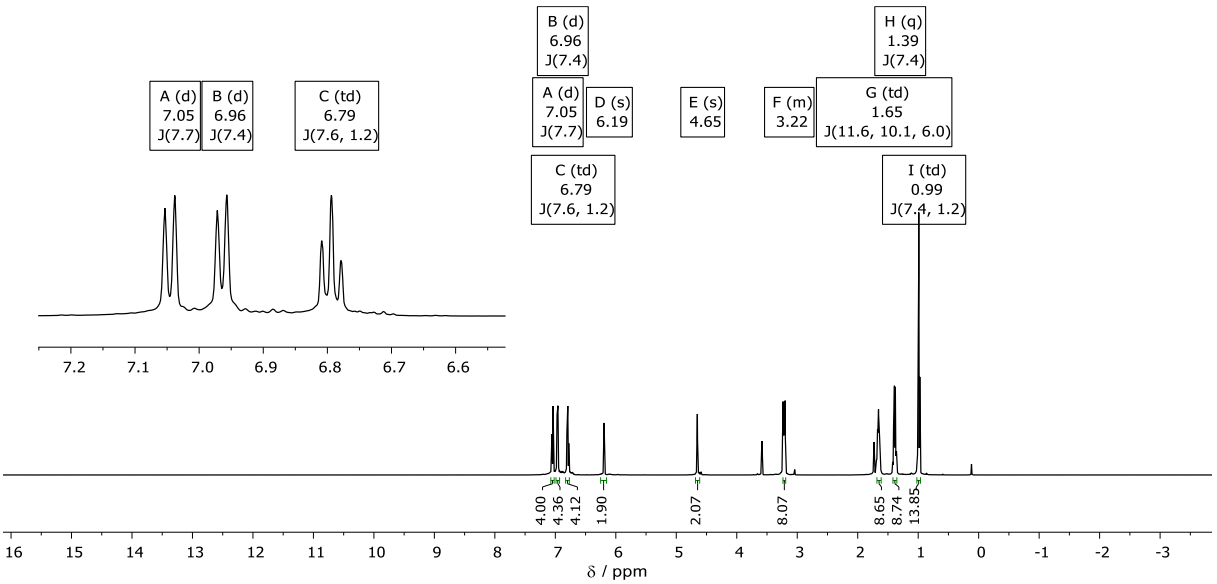

Figure S15. ^1H NMR spectrum of [**2**·I]$^-$[N^{n}Bu$_4$]$^+$ in THF-d_8.

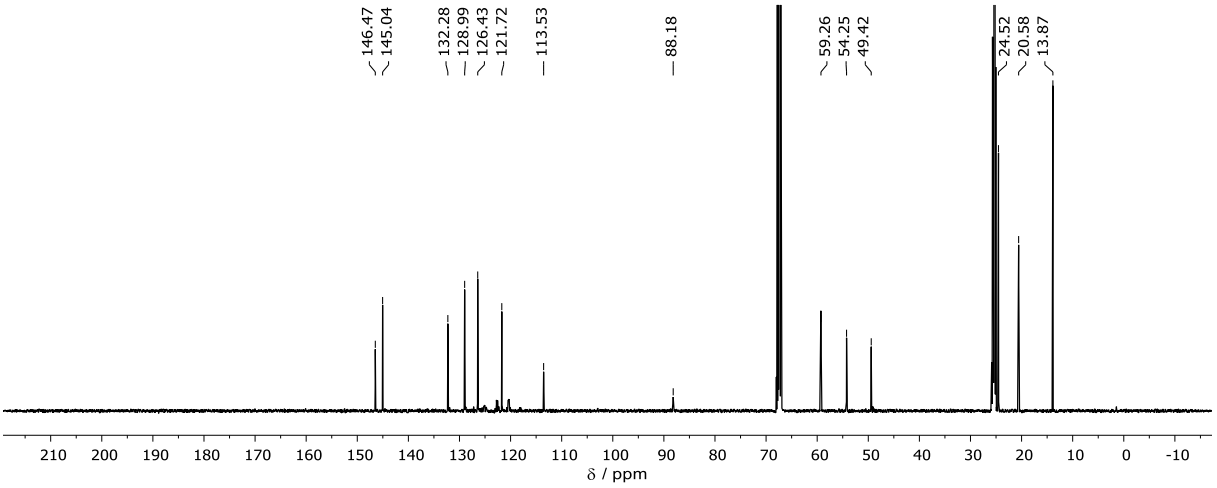

Figure S16. $^{13}C\{^{1}H\}$ NMR spectrum of [**2**·I]$^{-}$[N^{n}Bu$_4$]$^{+}$ in THF-d_8.

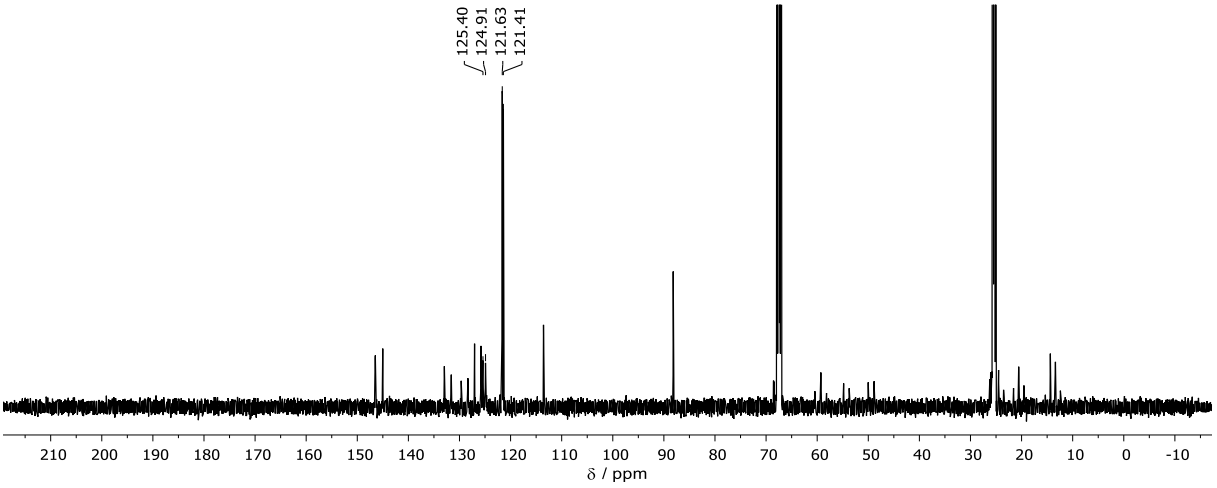

Figure S17. $^{13}C\{^{19}F\}$ NMR spectrum of [**2**·I]$^{-}$[N^{n}Bu$_4$]$^{+}$ in THF-d_8.

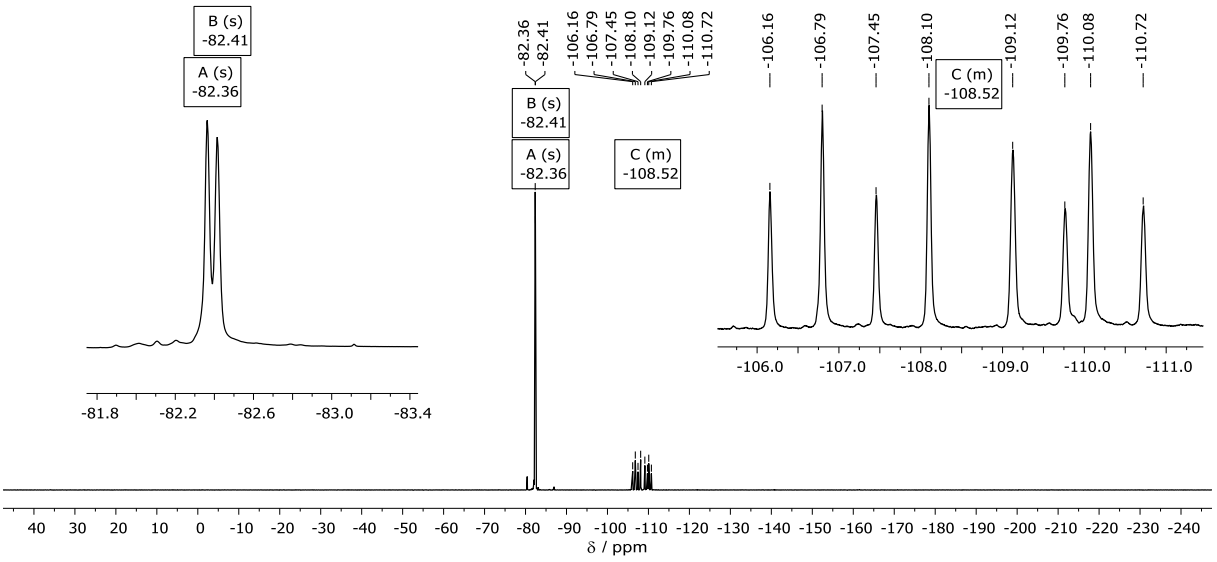

Figure S18. ^{19}F NMR spectrum of [**2**·I]$^{-}$[N^{n}Bu$_4$]$^{+}$ in THF-d_8.

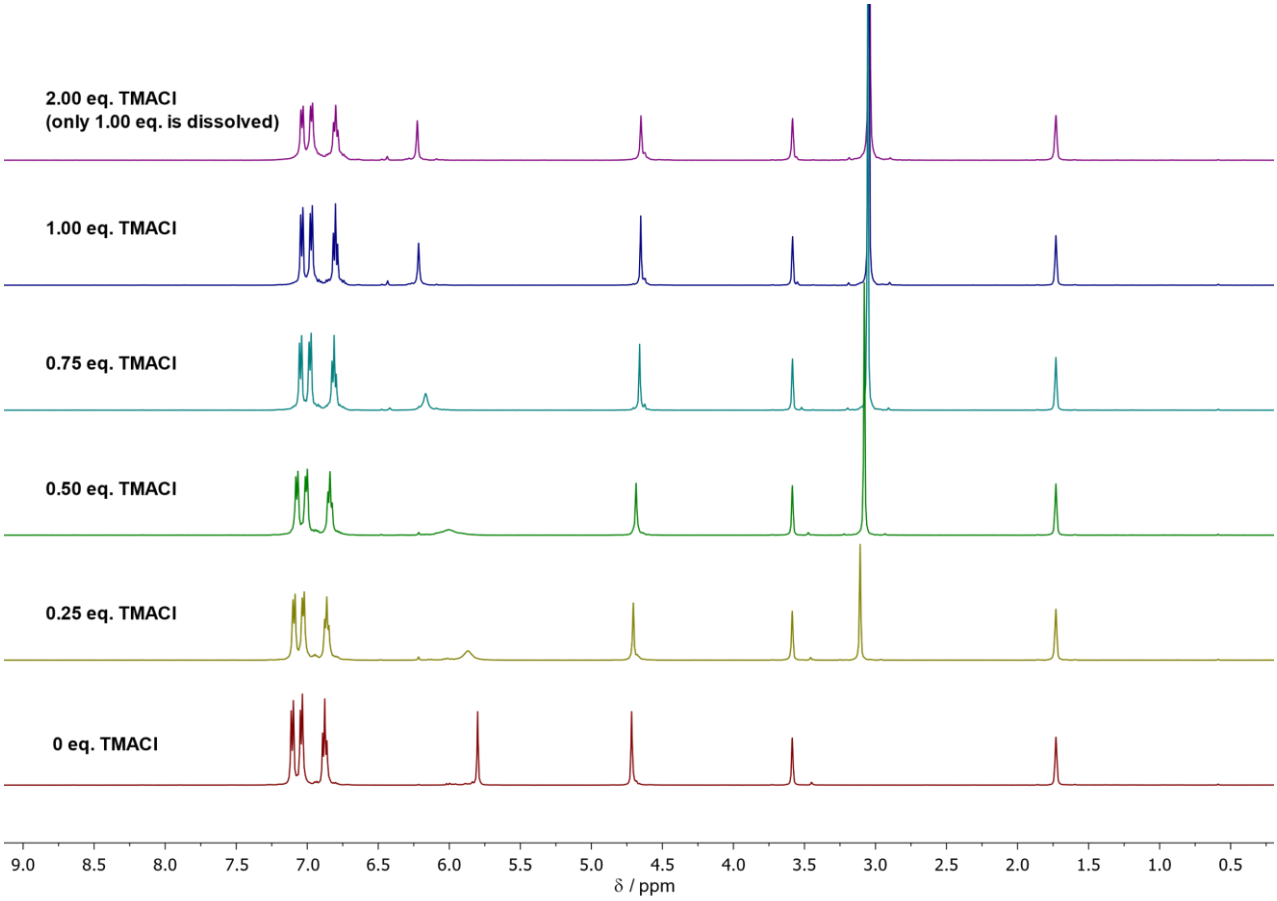

Figure S19. ^{1}H NMR spectra of the titration of **2** with TMACl in THF-d_8.

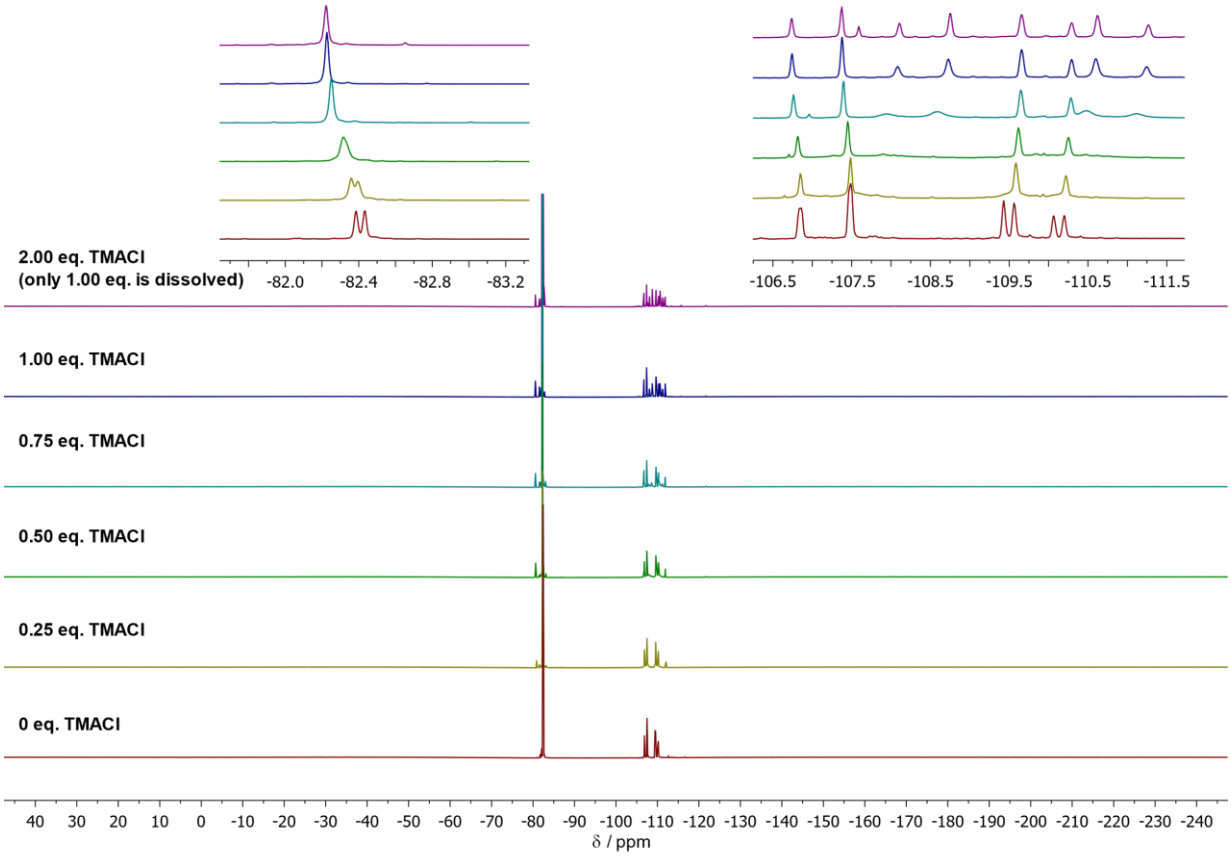

Figure S20. ^{19}F NMR spectra of the titration of **2** with TMACl in THF-d_8.

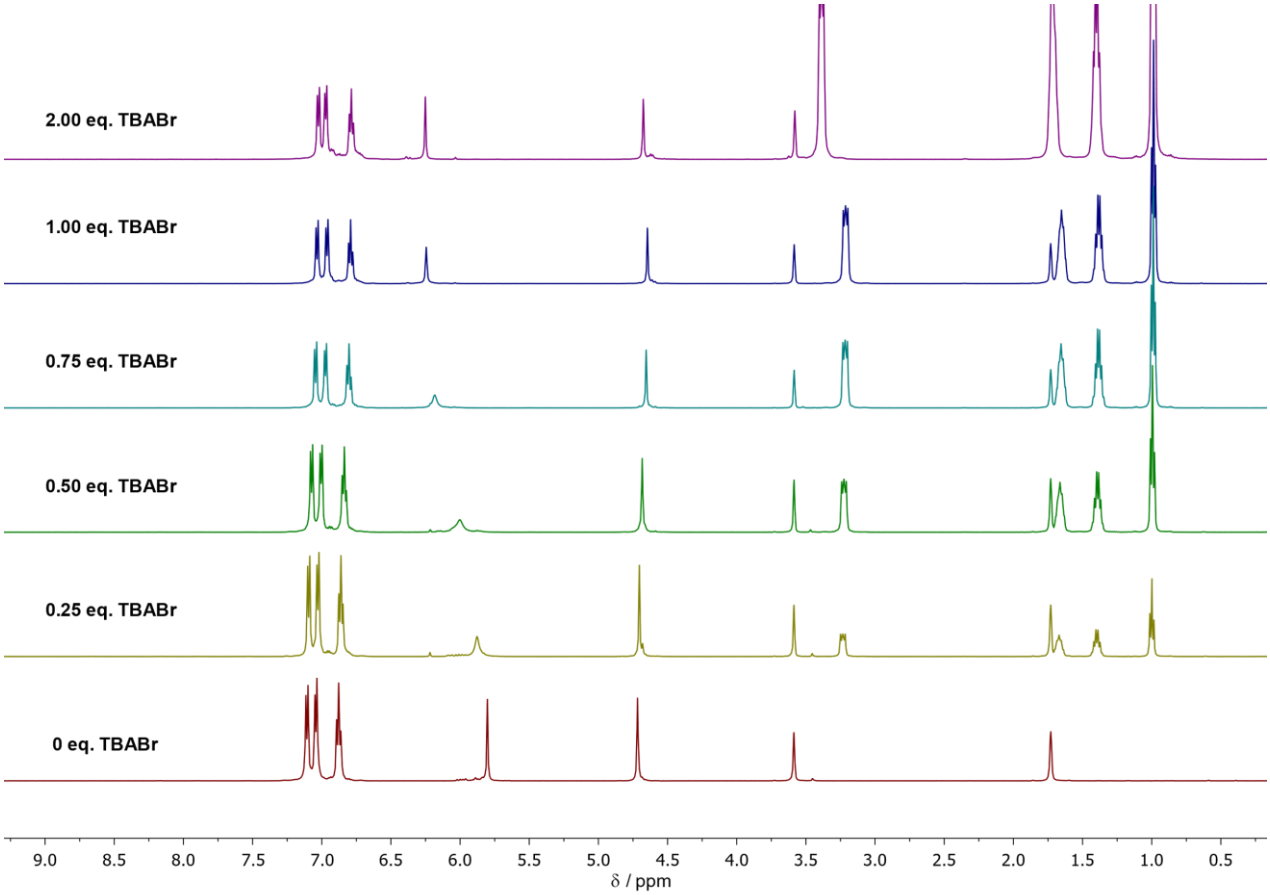

Figure S21. ^{1}H NMR spectra of the titration of **2** with TBABr in THF-d_8.

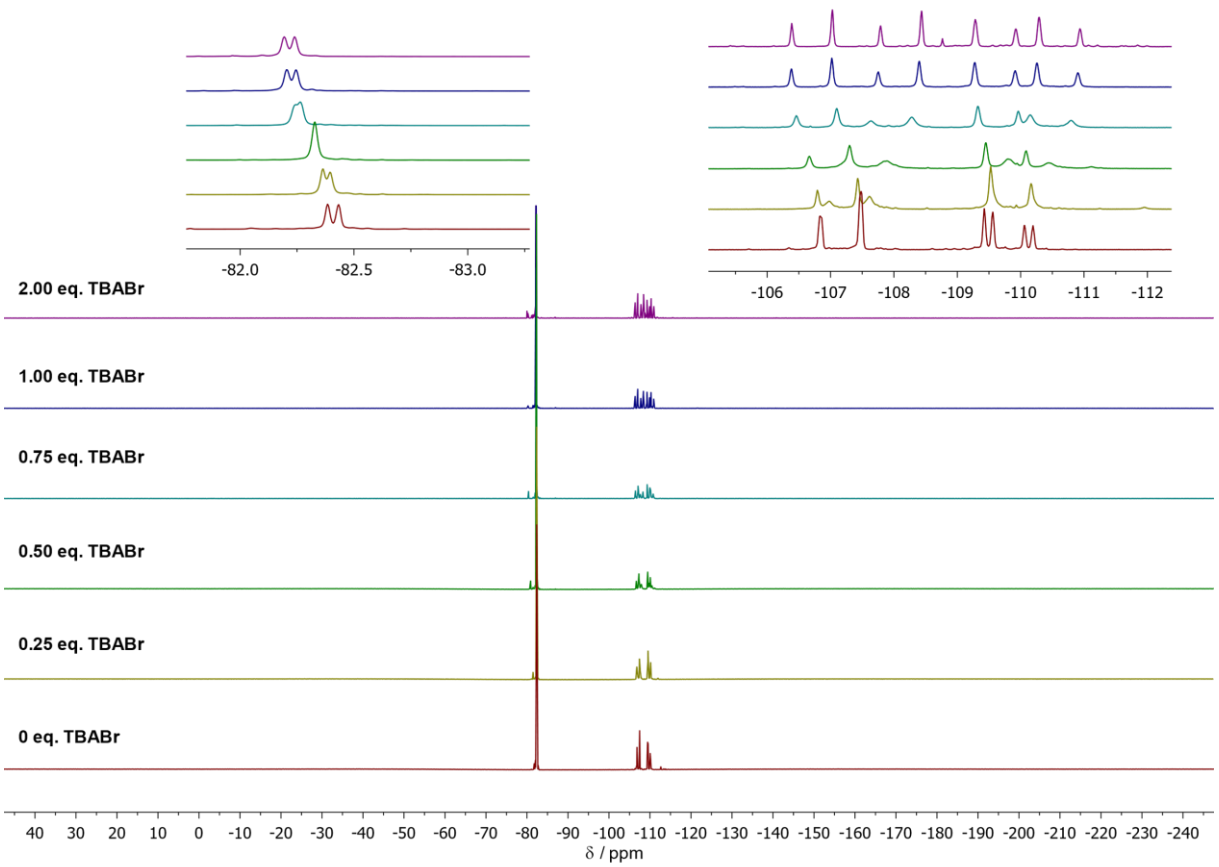

Figure S22. ^{19}F NMR spectra of the titration of **2** with TBABr in THF-d_8.

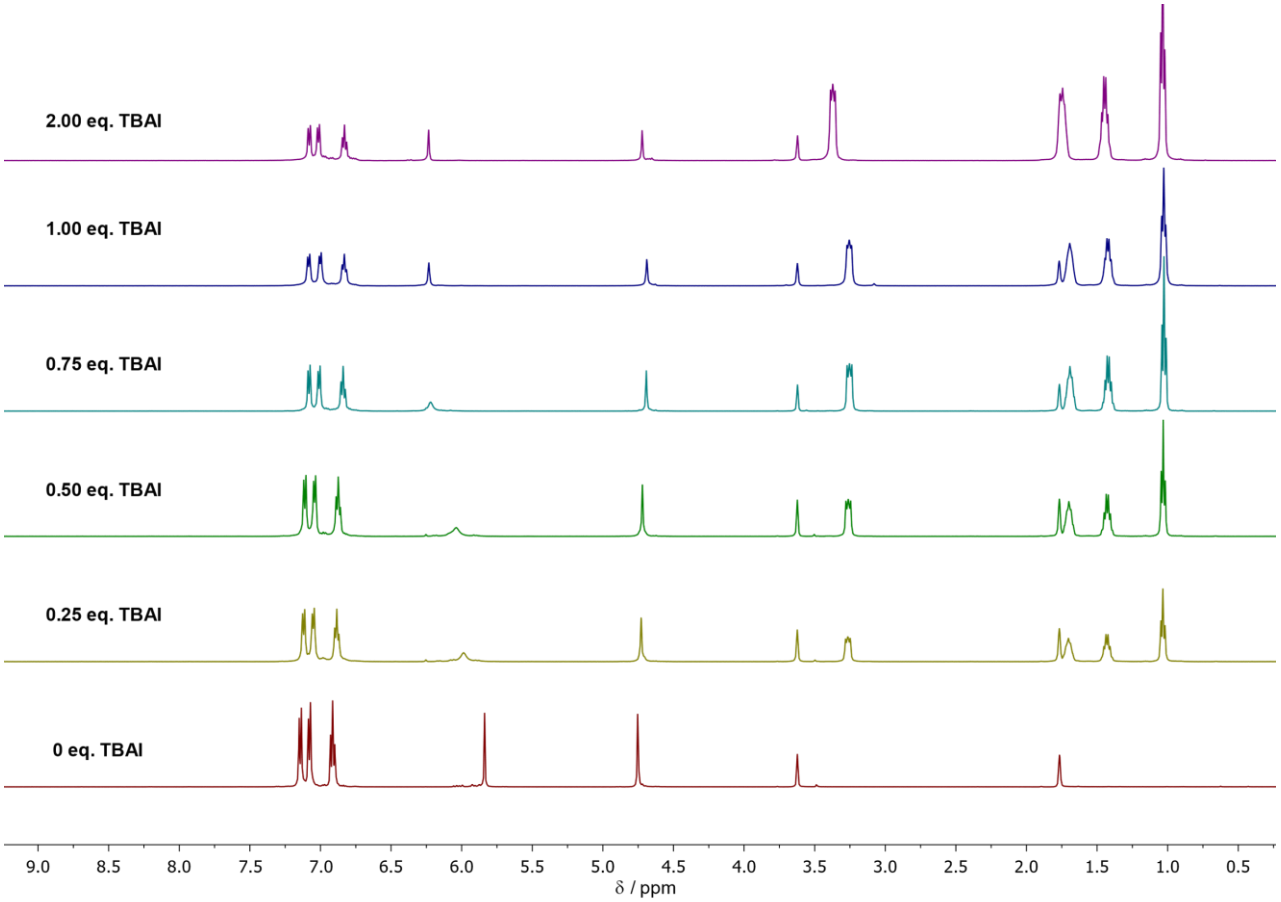

Figure S23. ^{1}H NMR spectra of the titration of **2** with TBAI in THF-d_8.

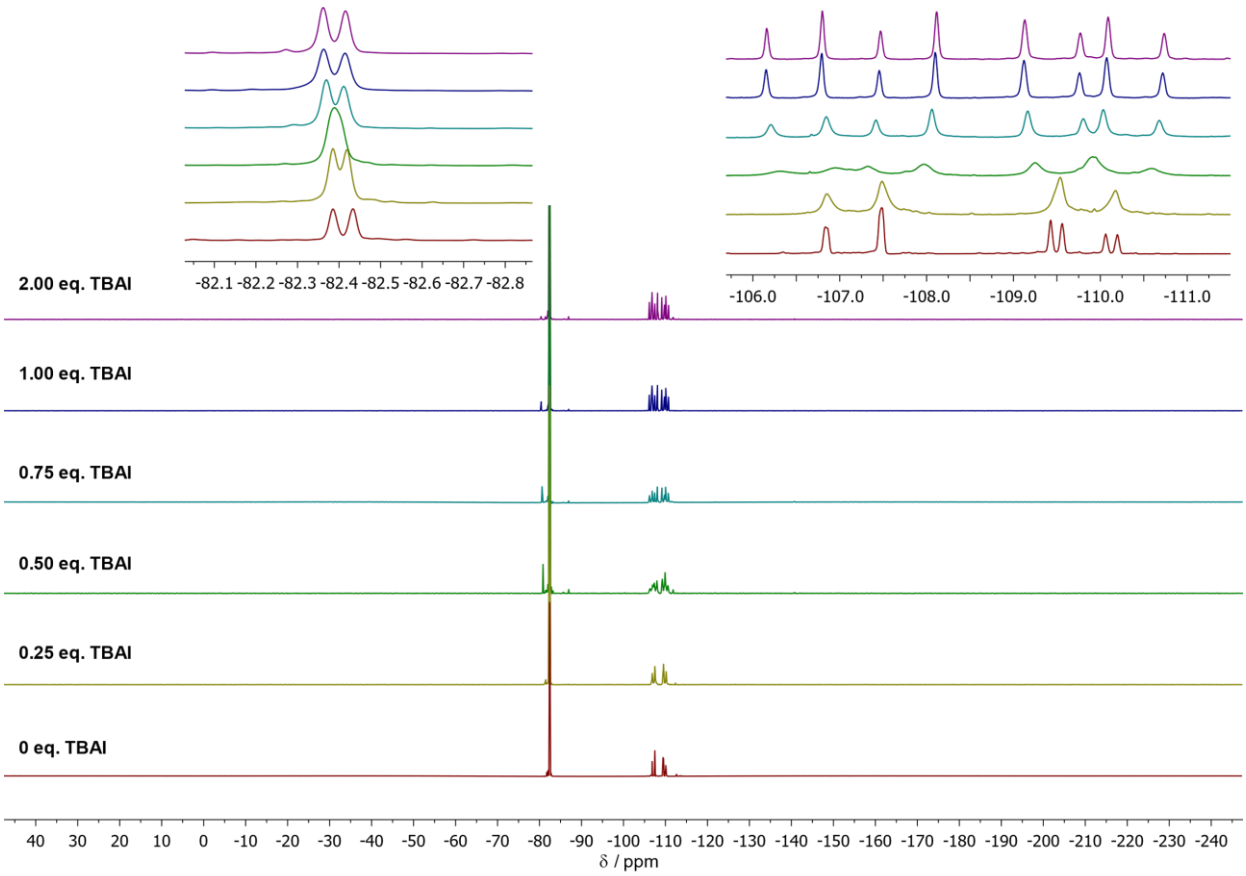

Figure S24. ^{19}F NMR spectra of the titration of **2** with TBAI in THF-d_8.

NMR spectroscopic data for competition reactions

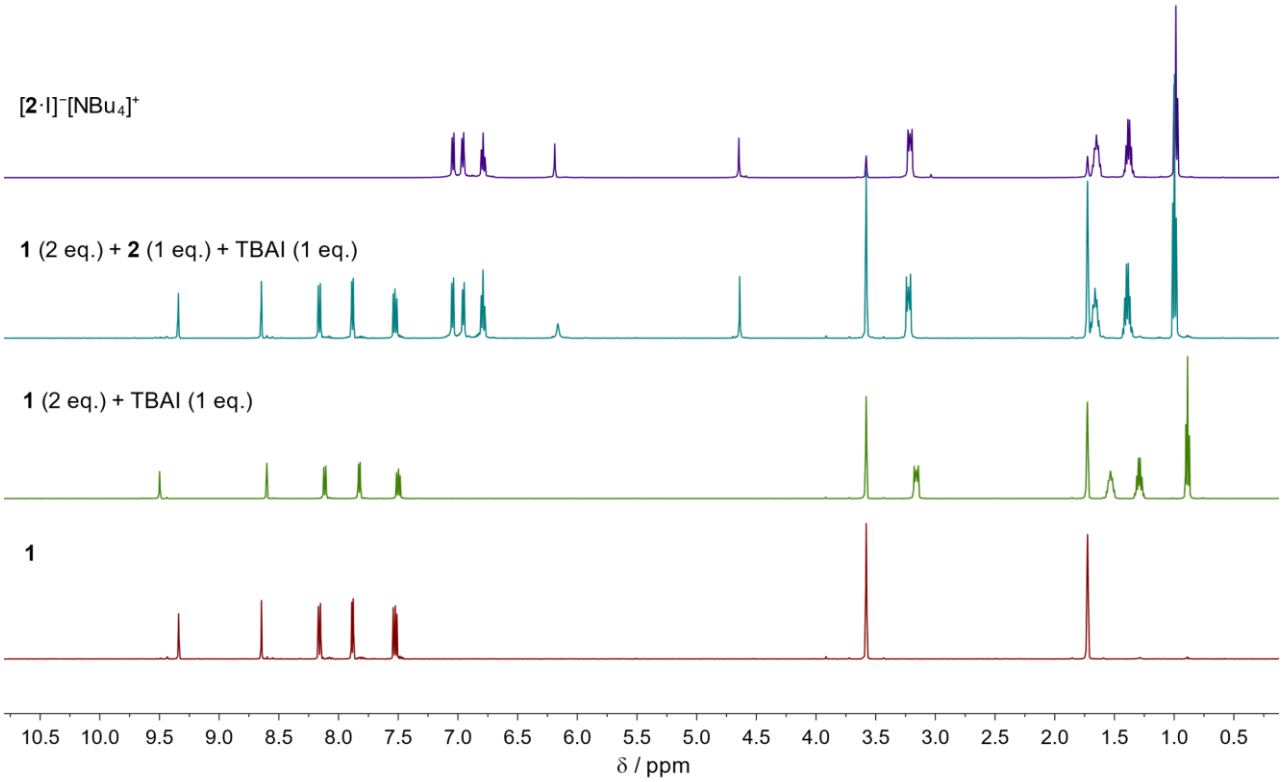

Figure S25. ^{1}H NMR spectra of the competition reaction of **1** and **2** with TBAI in THF-d_8.

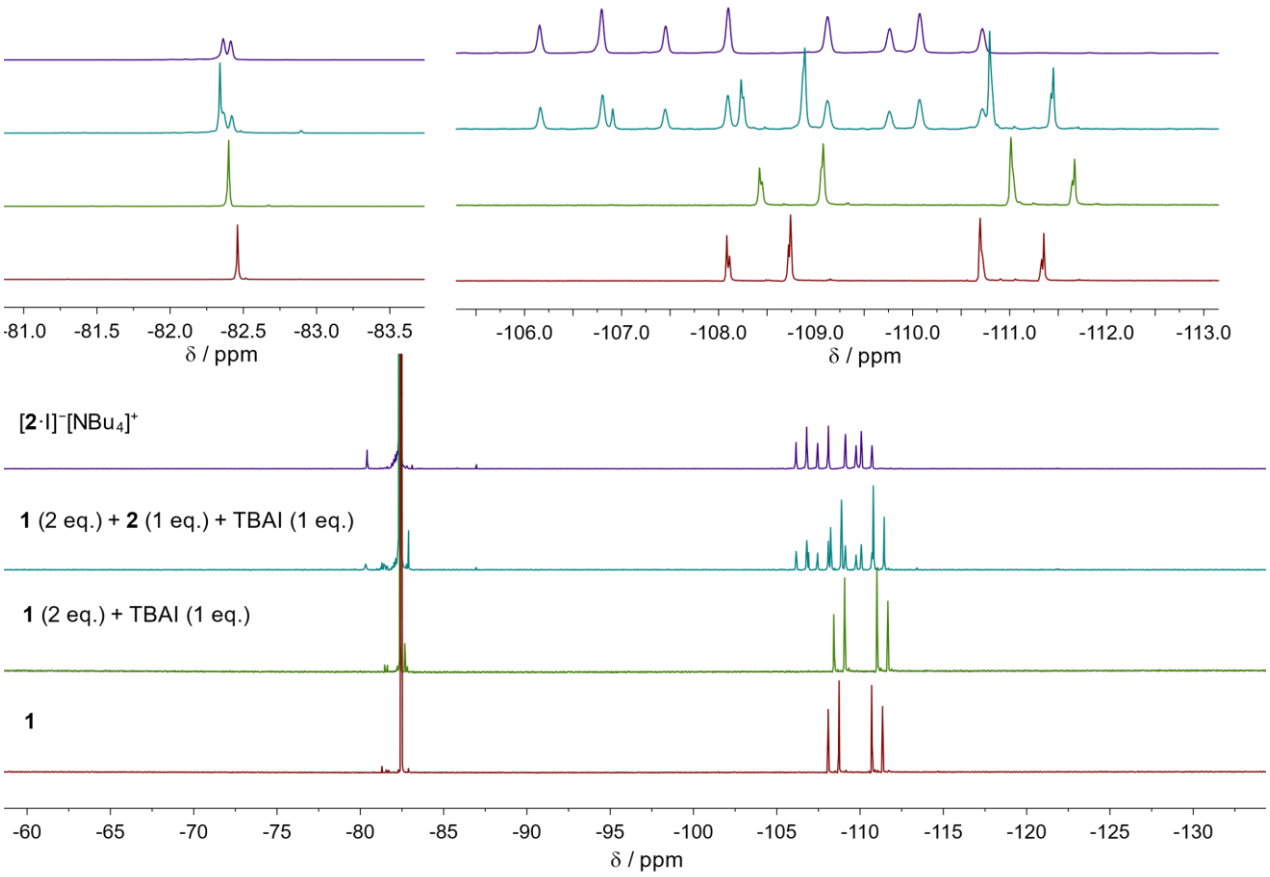

Figure S26. ^{19}F NMR spectra of the competition reaction of **1** and **2** with TBAI in THF-d_8.

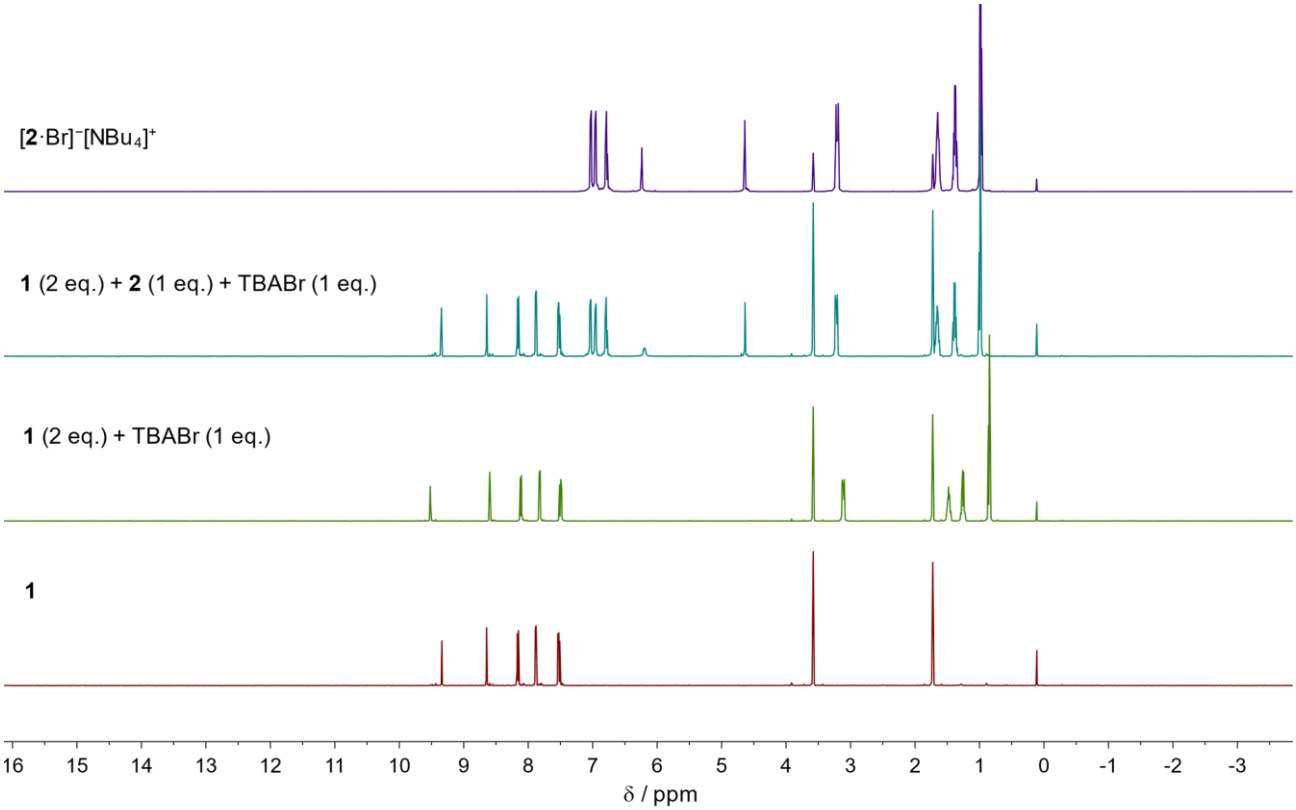

Figure S27. ^{1}H NMR spectra of the competition reaction of **1** and **2** with TBABr in THF-d_8.

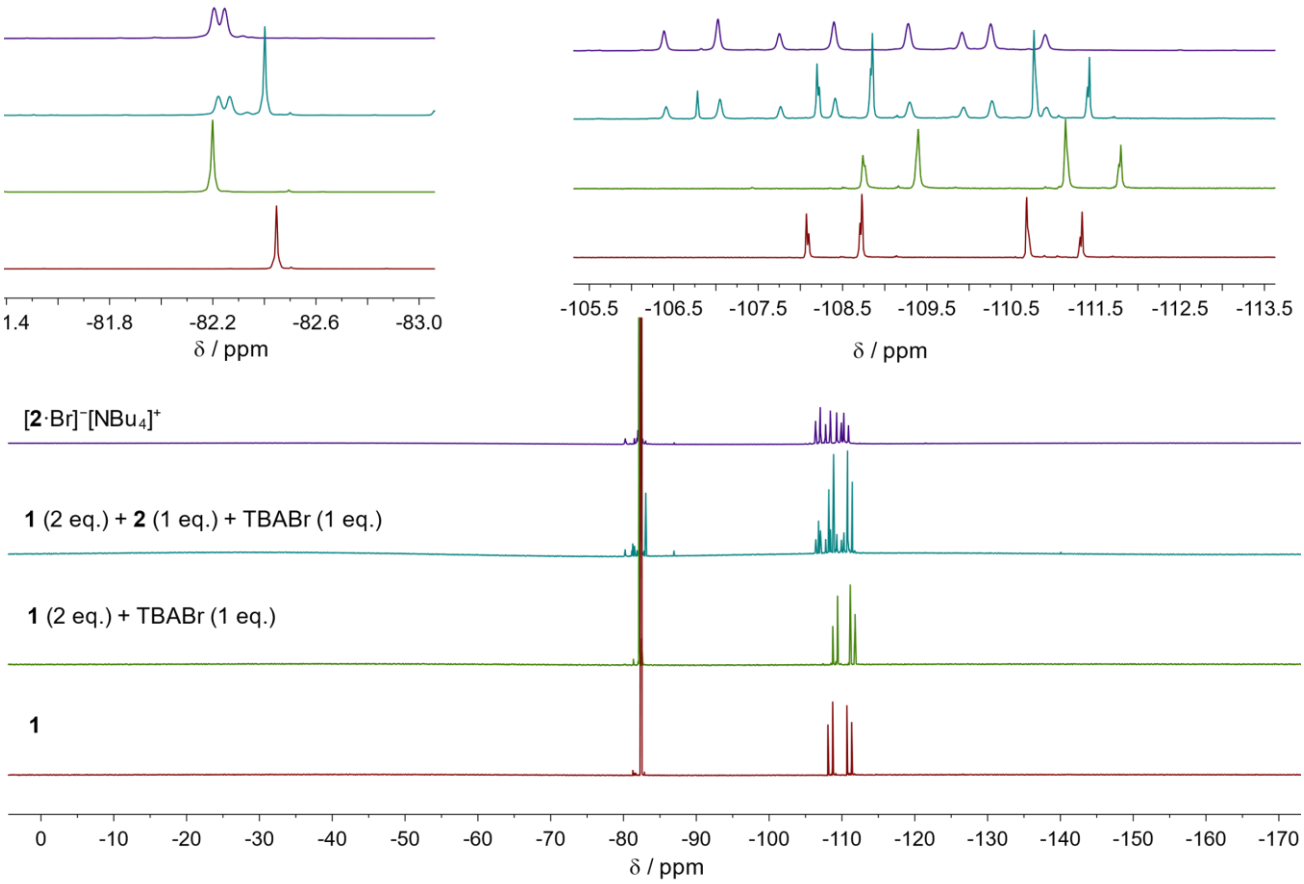

Figure S28. ^{19}F NMR spectra of the competition reaction of **1** and **2** with TBABr in THF-d_8.

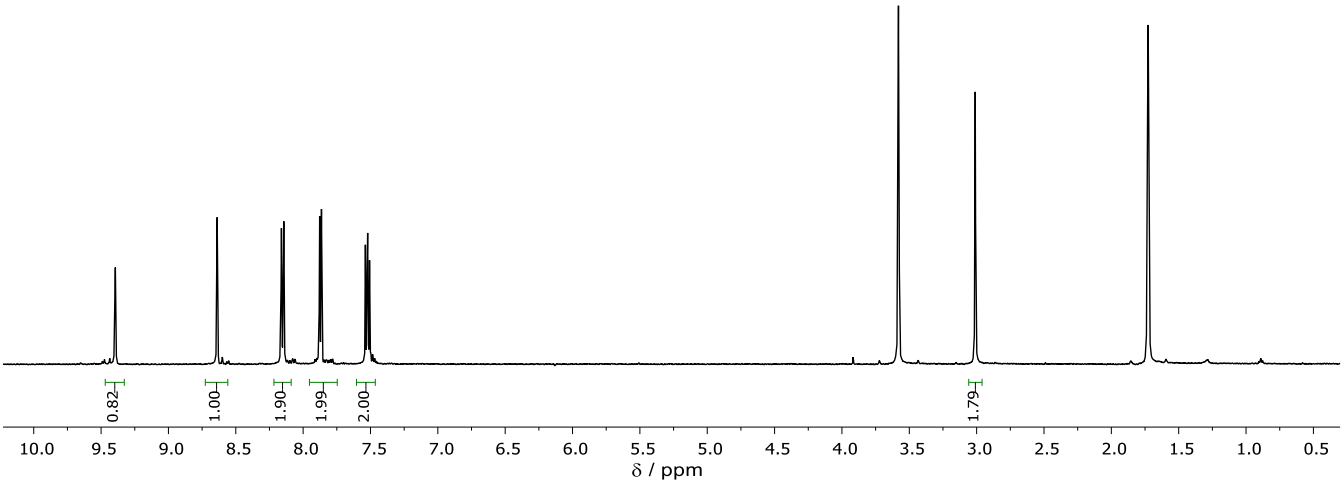

Figure S29. ^{1}H NMR spectrum of a mixture of **1** with TMACl (mostly undissolved) in THF-d_8.

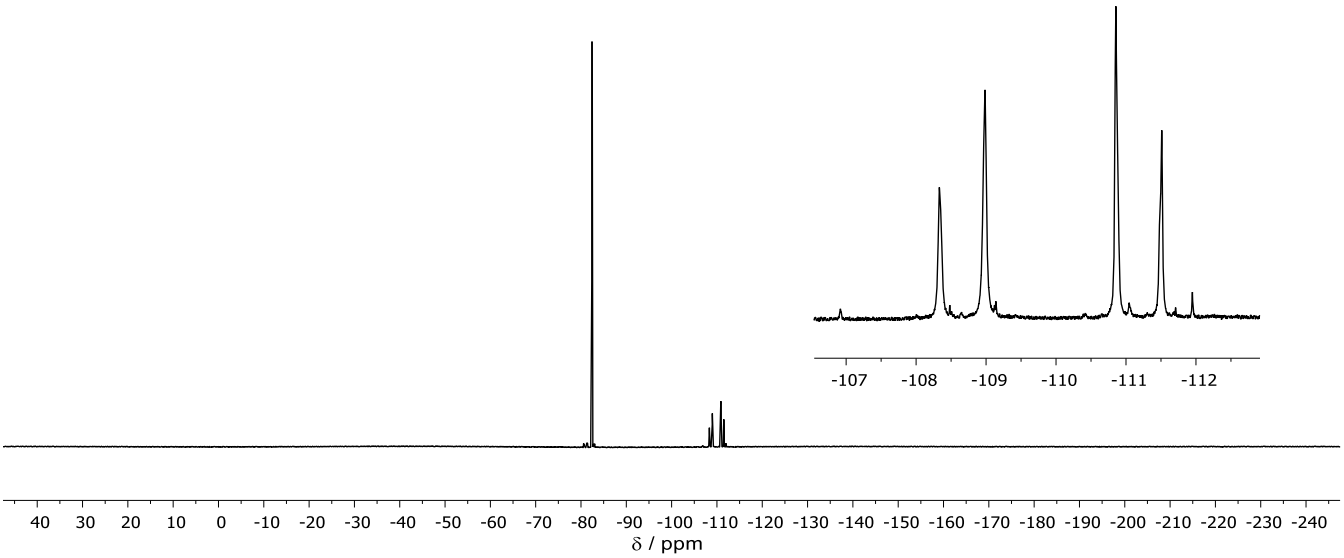

Figure S30. ^{19}F NMR spectrum of a mixture of **1** with TMACl in THF-d_8.

IR spectroscopic data

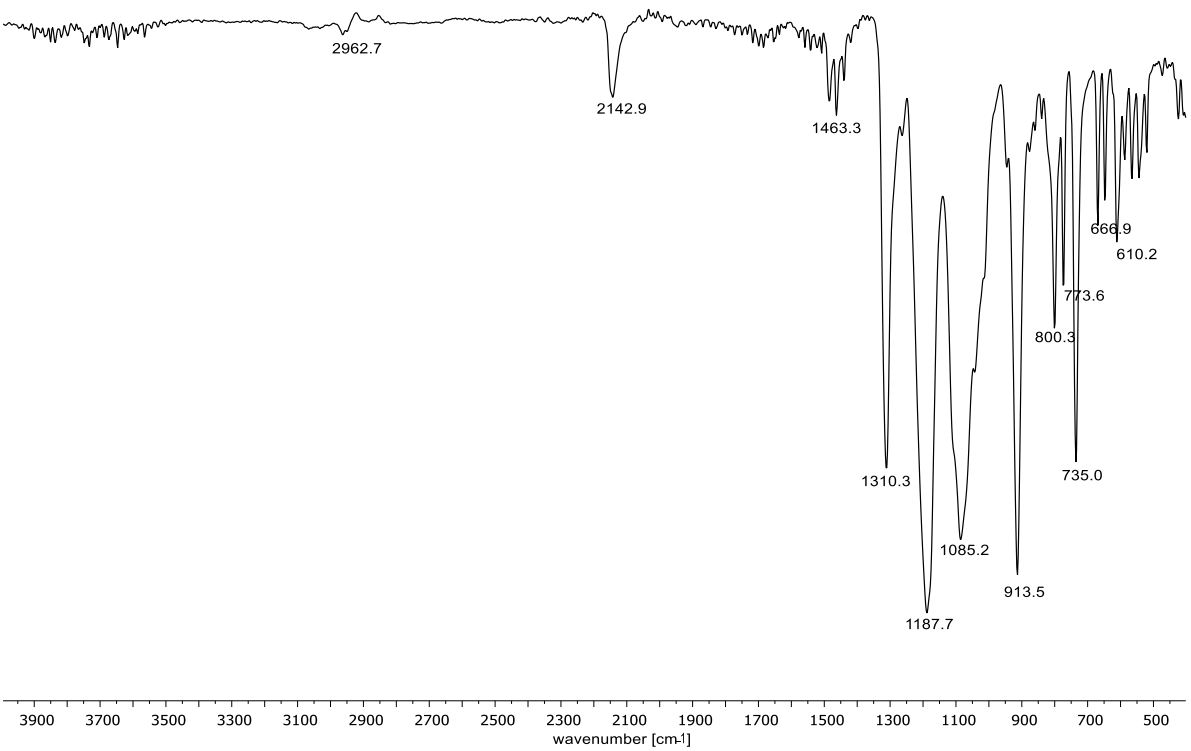

Figure S31. FT-IR spectrum of tetrastibanyl compound **2**.

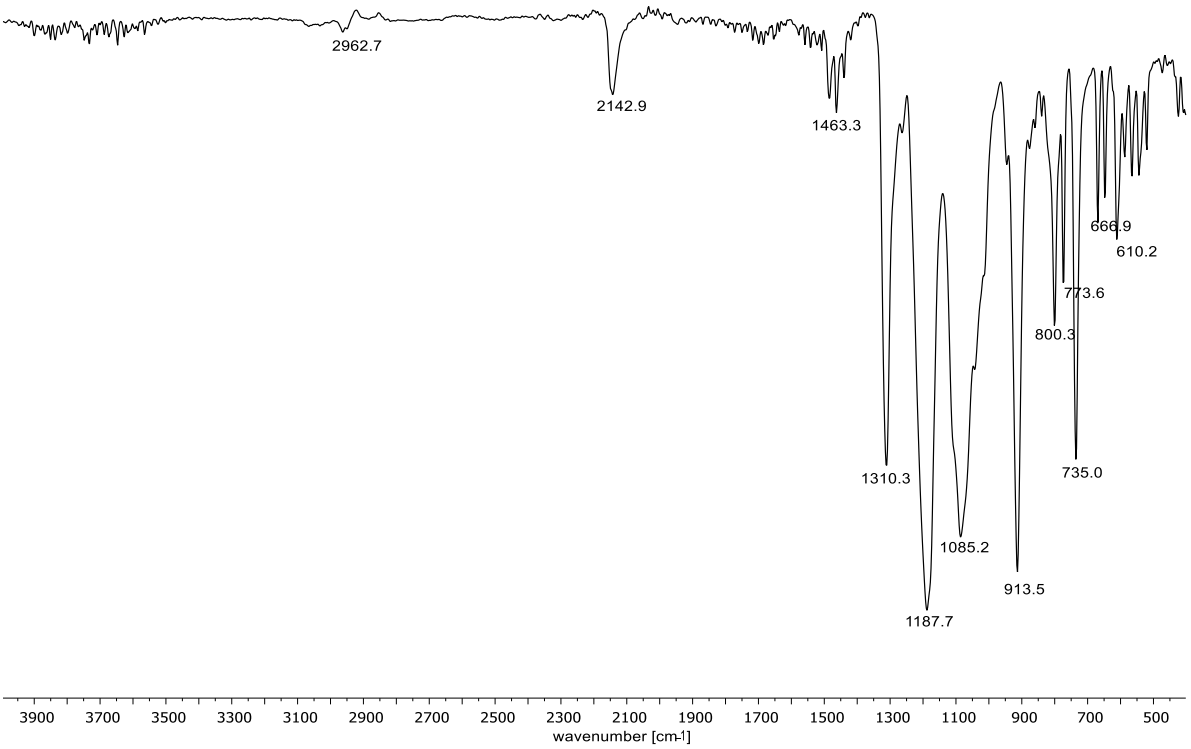

Figure S32. FT-IR spectrum of $[\mathbf{2}\cdot Cl]^{-}[NMe_4]^{+}$.

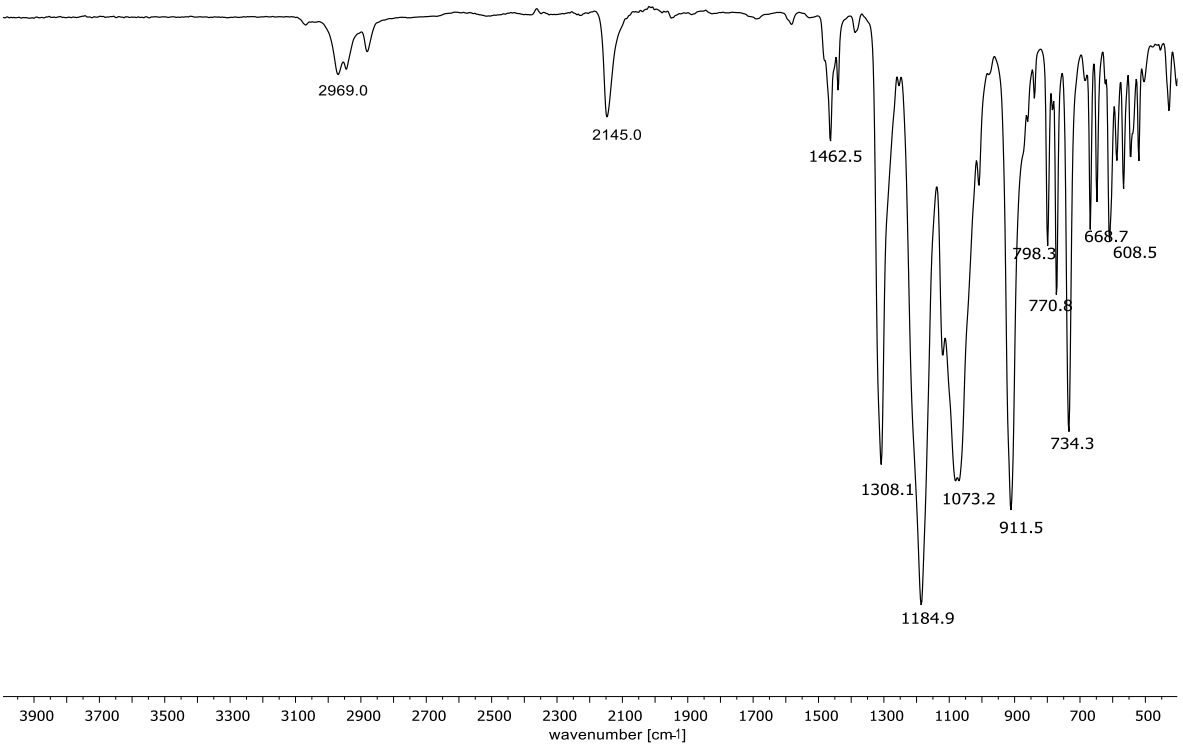

Figure S33. FT-IR spectrum of [**2**·Br]$^{-}$[N^{n}Bu$_4$]$^{+}$.

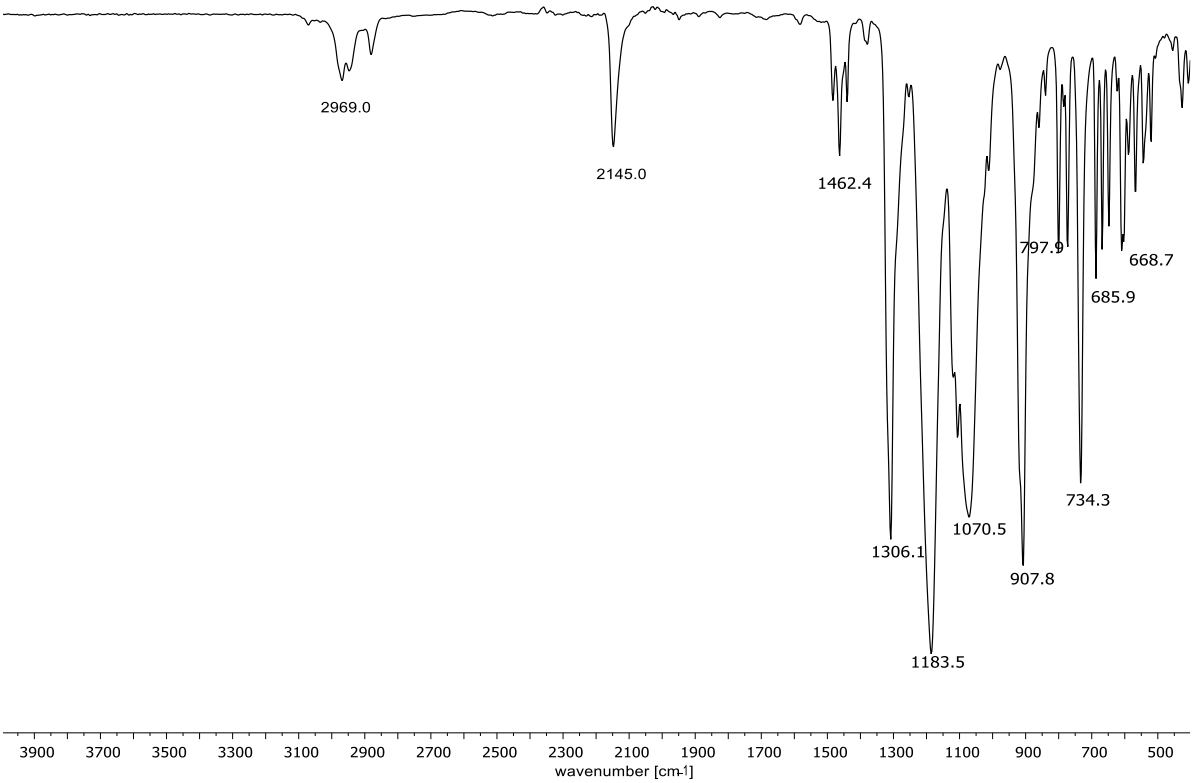

Figure S34. FT-IR spectrum of [**2**·I]$^{-}$[N^{n}Bu$_4$]$^{+}$.

Titration experiments for the determination of binding constants

Experimental procedures of the titration experiments

Titration experiments were performed by adding increasing amounts of halide salt (TBACl, TBABr, TBAI) to a solution of host **2** (40 mg, 21.2 µmol) in THF-d_8 (0.6 mL) in a Young-NMR tube. The TBAX salts (X = Cl, Br, I) were added as solids to keep the host concentration constant in the course of the titration. After each addition, the sample was analyzed by ^{1}H NMR (300 MHz) and ^{19}F NMR (282 MHz) spectroscopy. To reference the ^{19}F NMR spectra more precisely, a capillary with $CFCl_3$ (0.00 ppm) was added as an internal standard. The stacked ^{1}H and ^{19}F NMR titration spectra are provided further below in Figures S36 – S38.

The exact equivalents of added salt in each titration step were determined by the integration of the ^{1}H NMR spectra. In course of the titration, the CF_3 groups NMR signal showed almost no shift, which is why it was not useful for tracking the adduct formation. The NMR signals of the CF_2 groups were also unusable, since in the range of the most pronounced change (0 – 1.0 eq.) the determination of the shift was complicated by the peculiarly broadened signal pattern formed in the presence of sub-stochiometric amounts of TBAX (compare Fig. 2 in the main text). The only suitable signal was the ^{1}H NMR signal of the bridgehead protons H9/ H9', which are directed into the host's cavity. The equivalents and ^{1}H NMR shifts for each titration are provided in Table S1. A graph showing the chemical shift *versus* equivalents of halide salt is provided in Figure S35.

Calculation of the binding constants

The host-guest species are in rapid equilibrium and the exchange reactions were found to be fast on the NMR timescale. In general, the host-guest formations are suitable for the determination of binding constants by NMR chemical shift data. The total chemical shift (up to about 0.5 ppm) is large enough to calculate binding constants.

The concentrations of added guest and the corresponding chemical shift data were entered into the program Win EQNMR 2.[3] By estimating an initial binding constant and values of the chemical shifts of a saturated and uncomplexed host, the parameters were refined. The refinement applied non-linear least-squares analyses to obtain the best fit between empirical and calculated data. By variating the input parameters till convergence of the best fit values, binding constants were obtained. The data were found to be consistent with the assumption of a 1:1 host-guest stoichiometry. However, the titration graph does not perfectly correspond to a typical curve of a binding isotherm. As seen in Figure S35, there is almost no shift observable above 1.0 equivalents, and the data points up to 1.0 equivalents seem to correspond to a linear fit. This is why the errors of the calculated values of K_a are rather big. We assume this sharp bend at 1.0 equivalents to be the result of a rather high value of K_a along with the complex dynamics in the binding modes of the stibanyl functions of host **2**.

Table S1. Equivalents of halide salt determined by ^{1}H NMR integration and corresponding chemical shifts δ (in ppm) of the protons H9/ H9'.

TBACl		TBABr		TBAI	
eq.	δ	eq.	δ	eq.	δ
0	5.79	0	5.79	0	5.79
0.08	5.82	0.12	5.84	0.18	5.85
0.22	5.89	0.32	5.94	0.41	5.98
0.38	5.97	0.58	6.08	0.59	6.06
0.55	6.06	0.63	6.11	0.69	6.11
0.68	6.12	0.69	6.13	0.72	6.12
0.8	6.17	0.82	6.18	0.85	6.16
0.93	6.22	1.01	6.24	0.97	6.18
1.04	6.25	1.11	6.25	1.07	6.19
1.24	6.26	1.21	6.25	1.25	6.19
1.44	6.26	1.37	6.25	1.43	6.19
1.61	6.26	1.65	6.25	1.61	6.19
2.23	6.26	2.67	6.25	1.93	6.19

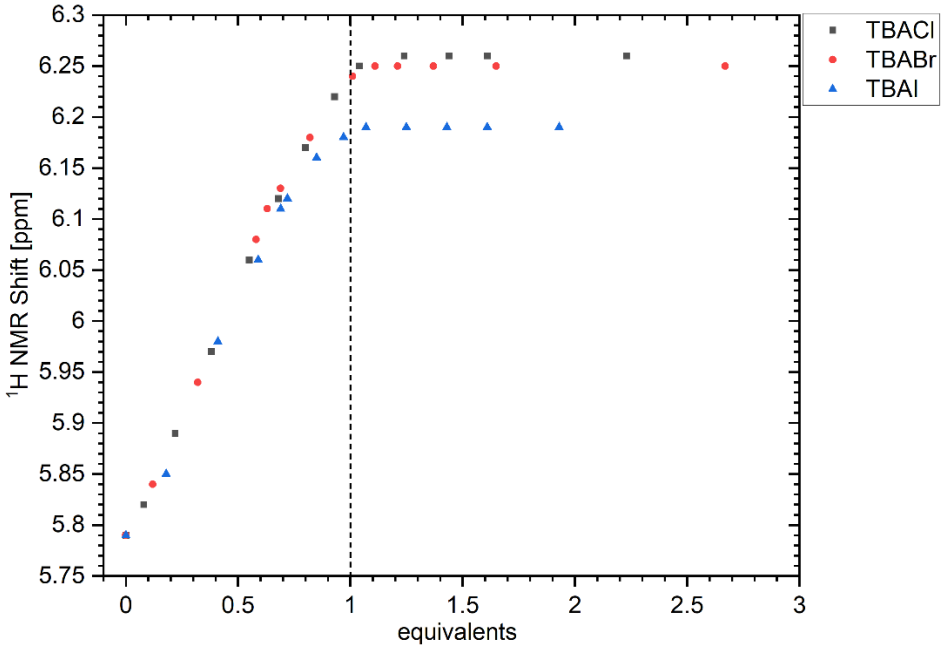

Figure S35. ^{19}F NMR shifts in course of a titration with guest (cf. data of Table S1).

NMR spectra of the titration experiments

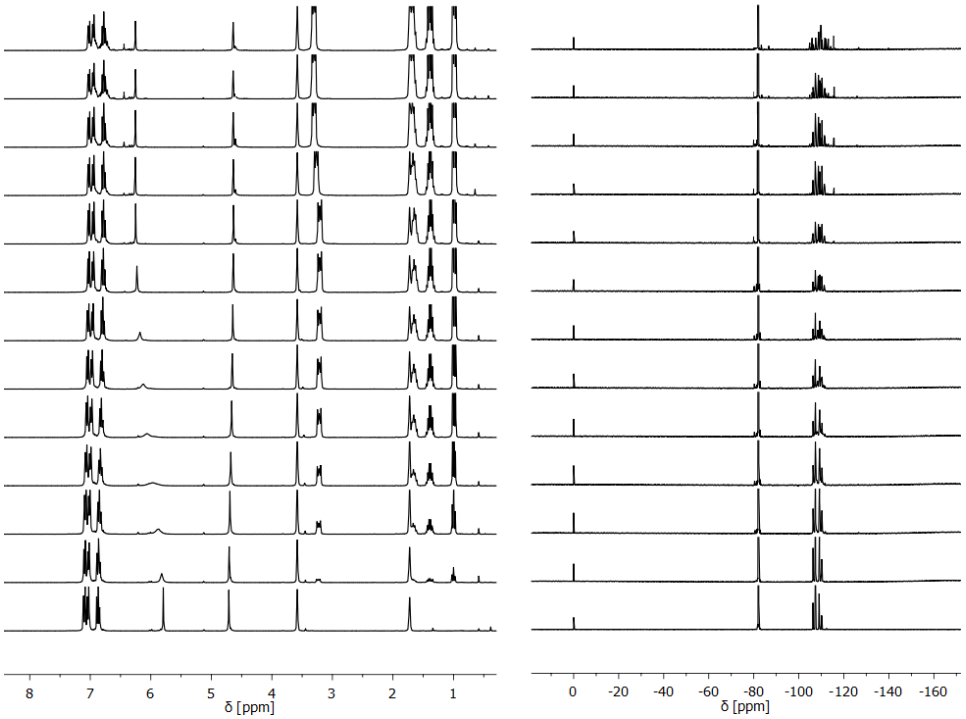

Figure S36. Stacked ^{1}H NMR spectra (left) and ^{19}F NMR spectra (right) of the titration experiments with TBACl in THF-d_8.

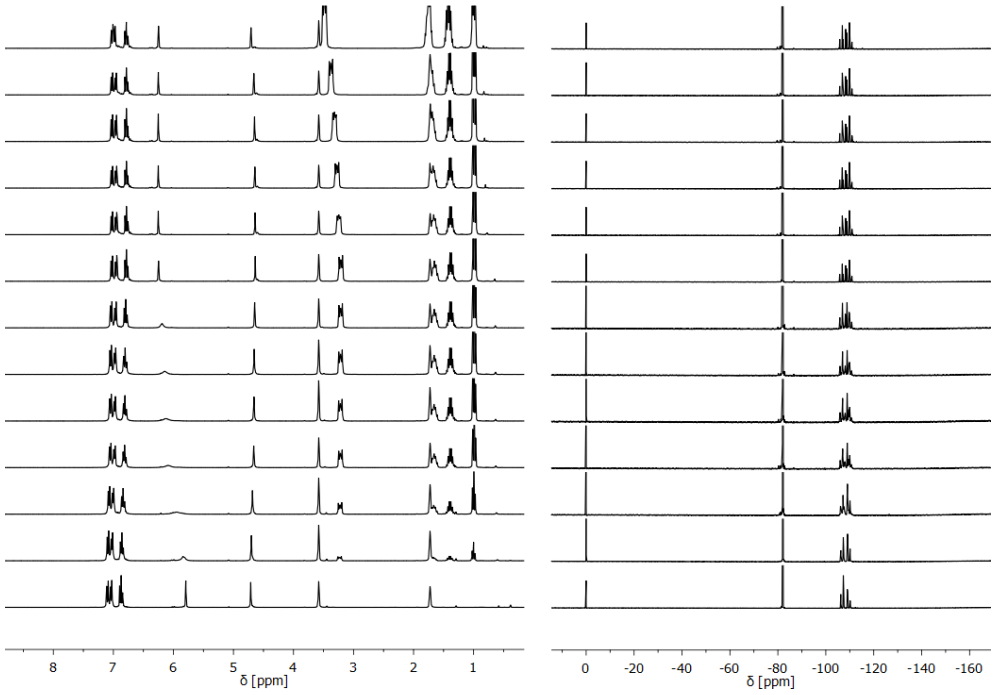

Figure S37. Stacked ^{1}H NMR spectra (left) and ^{19}F NMR spectra (right) of the titration experiments with TBABr in THF-d_8.

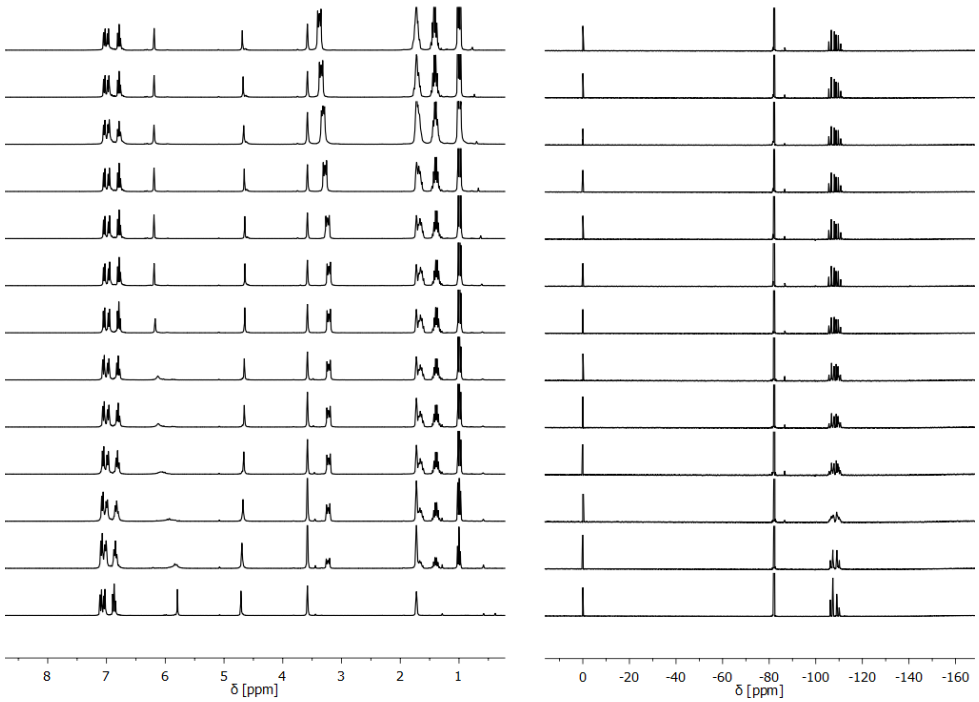

Figure S38. Stacked ^{1}H NMR spectra (left) and ^{19}F NMR spectra (right) of the titration experiments with TBAI in THF-d_8.

Crystallographic data

Single crystals were examined on a Rigaku Supernova diffractometer. The crystals were kept at 100.0(1) K during data collection. Using Olex2[4], the structures were solved with the ShelXT[5] structure solution program using Intrinsic Phasing and refined with the ShelXL[6] refinement package using Least Squares minimization.

2

Disorder of one C_2F_5 group over two sites in ratio 60:40. Bond lengths and angles were restrained using a well defined fragment. The ADP's were restrained with SIMU. The solvent CH_2Cl_2 is additionally disordered in ratio 81:19. Bond lengths were restrained with SADI, ADP's of the carbon with EADP.

[**2**·Cl]$^-$[NMe_4]$^+$

Disorder of four C_2F_5 groups over two sites in different ratios. These groups were treated as rigid groups with the geometry of a well defined fragment, their ADP's were restrained using RIGU and SIMU.

[**2**·Br]$^-$[N^nBu_4]$^+$

Hydrogen atoms were taken into account using a riding model. Some adp's of -CF_3 groups indicate disordering, but this could not be modelled reasonably.

[**2**·I]$^-$[N^nBu_4]$^+$

Disorder of one $Sb(C_2F_5)_2$ unit with ratio 93:7 and two C_2F_5 groups with ratio 1:1. Chemically equivalent bonds of the disordered parts were restrained to be same. Disordered atoms lying very close to each other were constrained to have the same thermal parameters.

Details of the X-ray investigation are given in Table S2. CCDC 2284089 – 2284092 contain the supplementary crystallographic data for this paper. These data can be obtained free of charge from The Cambridge Crystallographic Data Centre via https://www.ccdc.cam.ac.uk/structures.

Table S2. Crystallographic data for compounds **2**, [**2**·Cl]$^-$[NMe$_4$]$^+$, [**2**·Br]$^-$[N^{n}Bu$_4$]$^+$ and [**2**·I]$^-$[N^{n}Bu$_4$]$^+$.

Compound	**2**·CH_2Cl_2	[**2**·Cl]$^-$[NMe$_4$]$^+$·2 C_6H_6	[**2**·Br]$^-$[N^{n}Bu$_4$]$^+$·C_6H_6	[**2**·I]$^-$[N^{n}Bu$_4$]$^+$·C_6H_6
Empirical formula	$C_{53}H_{18}Cl_2F_{40}Sb_4$	$C_{68}H_{40}ClF_{40}NSb_4$	$C_{74}H_{58}BrF_{40}NSb_4$	$C_{74}H_{58}F_{40}INSb_4$
M_r	1972.57	2153.46	2288.12	2332.09
T [K]	100.0(1)	100.0(1)	100.0(1)	100.0(1)
Radiation	Mo Kα	Mo Kα	Mo Kα	Mo Kα
Crystal system	triclinic	monoclinic	monoclinic	triclinic
Space group	$P\bar{1}$	$P2_1/c$	$P2_1/n$	$P\bar{1}$
a [Å]	13.5356(6)	15.7731(2)	15.9954(5)	13.1683(2)
b [Å]	14.1129(5)	21.2235(4)	19.9387(5)	15.0933(2)
c [Å]	17.7477(6)	22.9543(4)	26.1599(6)	22.5113(3)
α [°]	79.806(3)	90	90	72.1222(14)
β [°]	77.865(3)	102.695(2)	103.584(2)	78.1365(13)
γ [°]	69.445(4)	90	90	83.5967(13)
Volume [Å^3]	3083.7(2)	7496.3(2)	8109.7(4)	4161.5(2)
Z	2	4	4	2
ρ_{calc} [g/cm^3]	2.124	1.908	1.874	1.861
μ [mm^{-1}]	1.979	1.603	1.946	1.787
F(000)	1868	4144	4432	2246
2Θ range [°]	3.102 – 60.162	3.27 – 52.044	4.904 – 60.068	4.532 – 60.068
Index ranges	−19 ≤ h ≤ 19 −19 ≤ k ≤ 19 −25 ≤ l ≤ 25	−19 ≤ h ≤ 19 −26 ≤ k ≤ 26 −28 ≤ l ≤ 28	−22 ≤ h ≤ 22 −28 ≤ k ≤ 28 −36 ≤ l ≤ 36	−18 ≤ h ≤ 18 −21 ≤ k ≤ 21 −31 ≤ l ≤ 31
Refl. collected	68786	117638	314023	276351
Independent refl.	18108	14779	23701	24364
R_{int}	0.0497	0.0472	0.0832	0.0503
Refl. with I >2σ(I)	13324	12520	17906	20916
Data / restraints / parameters	18108 / 78 / 912	14799 / 704 / 1167	23701 / 0 / 1085	24364 / 2083 / 1299
Goodness-of-Fit on F^2	1.057	1.058	1.059	1.050
R_1/wR_2 [I > 2σ(I)]	0.0543 / 0.1260	0.0885 / 0.2426	0.0539 / 0.1284	0.0337 / 0.0819
R_1/wR_2 (all data)	0.0815 / 0.1428	0.0988 / 0.2530	0.0793 / 0.1455	0.0417 / 0.0860
ρ_{fin} (max/min) [e Å^{-3}]	2.08 / −1.66	5.44 / −2.39	3.80 / −1.15	2.02 / −1.05
CCDC	2284089	2284090	2284091	2284092

Additional data for Figure 4

The data for Figure 4, which were taken from the solid-state structures of [**2**·Cl]$^-$[NMe$_4$]$^+$, [**2**·Br]$^-$[N^{n}Bu$_4$]$^+$ and [**2**·I]$^-$[N^{n}Bu$_4$]$^+$, are listed in Table S3. The *van der Waals* and covalent radii sums given by literature[7-9] are $\sum r_{vdW}$(Sb, Cl) = 3.81 Å, $\sum r_{vdW}$(Sb, Br) = 3.89 Å, $\sum r_{vdW}$(Sb, I) = 4.04 Å, $\sum r_{cov}$(Sb, Cl) = 2.39 Å, $\sum r_{cov}$(Sb, Br) = 2.54 Å, $\sum r_{cov}$(Sb, I) = 2.73 Å). The indication of an elongation of the Sb–C^F bond given in Figure 4 refers to a comparison with the longest of all eight Sb–C^F bonds in the free host **2**, which is 2.244(6) Å.

Table S3: Selected distances [Å] and angles [°] of the solid state structures of [**2**·Cl]$^-$[NMe$_4$]$^+$, [**2**·Br]$^-$[N^{n}Bu$_4$]$^+$ and [**2**·I]$^-$[N^{n}Bu$_4$]$^+$, which were used for Figure 4. In case of a disorder in the structure, the values of the molecule of higher occupancy are given. In each case, the X···Sb–C^F motif with the larger angle was selected.

Adduct	X···Sb–C^F	*d* (X···Sb) [Å]	*d* (Sb–C^F) [Å]	∠ X···Sb–C^F [°]
[**2**·Cl]$^-$[NMe$_4$]$^+$	Cl-Sb(1)-C(17)	3.055(3)	2.302(13)	165.8(3)
	Cl-Sb(2)-C(23)	4.082(3)	2.252(10)	139.4(3)
	Cl-Sb(3)-C(45)	3.580(3)	2.242(5)	146.7(2)
	Cl-Sb(4)-C(49)	2.951(3)	2.362(10)	170.5(3)
[**2**·Br]$^-$[N^{n}Bu$_4$]$^+$	Br-Sb(1)-C(37)	3.140(1)	2.304(5)	177.8(1)
	Br-Sb(2)-C(41)	3.737(1)	2.255(5)	135.6(1)
	Br-Sb(3)-C(45)	3.975(1)	2.248(5)	146.6(2)
	Br-Sb(4)-C(51)	3.189(1)	2.267(5)	171.4(1)
[**2**·I]$^-$[N^{n}Bu$_4$]$^+$	I-Sb(1)-C(37)	3.498(1)	2.276(3)	167.8(1)
	I-Sb(2)-C(41)	3.456(1)	2.274(3)	170.1(1)
	I-Sb(3)-C(47)	3.561(1)	2.311(19)	175.3(3)
	I-Sb(4)-C(51)	3.909(1)	2.242(3)	139.6(1)

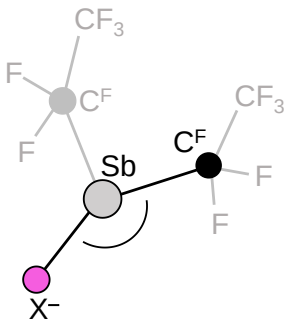

Aryl-aryl interactions below 4 Å

2

Plane #1: C1 C14 C13 C12 C11 C2
Plane #2: C3 C4 C9 C10 C11 C2
Plane #3: C29 C30 C35 C36 C37 C28
Plane #4: C5 C6 C7 C8 C9 C4
Plane #5: C28 C37 C38 C39 C40 C27
Plane #6: C31 C32 C33 C34 C35 C30

Considering plane #1
#1@2_666 (1-X,1-Y,1-Z)
angle: 0.000, centroid-centroid distance: 3.644, shift distance 1.002
#3@1_555 (+X,+Y,+Z)
angle: 47.946, centroid-centroid distance: 3.715, shift distance 1.492

Considering plane #2
#4@1_555 (+X,+Y,+Z)
angle: 54.736, centroid-centroid distance: 3.874, shift distance 1.736

Considering plane #3
#3@2_656 (1-X,-Y,1-Z)
angle: 0.000, centroid-centroid distance: 3.750, shift distance 0.958

Considering plane #4
No interactions found

Symmetry codes:
1_555 +X,+Y,+Z
2_555 -X,-Y,-Z

[**2**·Cl]$^{-}$[NMe$_4$]$^{+}$

Plane #1: C1 C14 C13 C12 C11 C2
Plane #2: C2 C11 C10 C9 C4 C3
Plane #3: C29 C30 C35 C36 C37 C28
Plane #4: C5 C6 C7 C8 C9 C4
Plane #5: C28 C37 C38 C39 C40 C27
Plane #6: C31 C32 C33 C34 C35 C30
Plane #7: C57 C62 C61 C60 C59 C58
Plane #8: C63 C68 C67 C66 C65 C64

Considering plane #1
#3@1_555 (+X,+Y,+Z)
angle: 47.373, centroid-centroid distance: 3.713, shift distance 1.518

Considering plane #2
#4@1_555 (+X,+Y,+Z)
angle: 52.556, centroid-centroid distance: 3.831, shift distance 1.737

Considering plane #3
No interactions found

Considering plane #4
No interactions found

Considering plane #5
No interactions found

Considering plane #6
No interactions found

Symmetry codes:
1_555 +X,+Y,+Z
2_555 -X,0.5+Y,0.5-Z
3_555 -X,-Y,-Z
4_555 +X,-0.5-Y,-0.5+Z

[**2**·Br]$^{-}$[N^{n}Bu$_4$]$^{+}$

Plane #1: C1 C14 C13 C12 C11 C2
Plane #2: C3 C4 C9 C10 C11 C2
Plane #3: C17 C18 C23 C24 C25 C16
Plane #4: C5 C6 C7 C8 C9 C4
Plane #5: C16 C25 C26 C27 C28 C15
Plane #6: C19 C20 C21 C22 C23 C18
Plane #7: C69 C74 C73 C72 C71 C70

Considering plane #1
#3@1_555 (+X,+Y,+Z)
angle: 44.996, centroid-centroid distance: 3.654, shift distance 1.430

Considering plane #2
#4@1_555 (+X,+Y,+Z)
angle: 43.117, centroid-centroid distance: 3.594, shift distance 1.431

Considering plane #3
No interactions found

Considering plane #4
No interactions found

Considering plane #5
No interactions found

Symmetry codes:
1_555 +X,+Y,+Z
2_555 0.5-X,0.5+Y,0.5-Z
3_555 -X,-Y,-Z
4_555 -0.5+X,-0.5-Y,-0.5+Z

[**2**·I]$^{-}$[N^{n}Bu$_4$]$^{+}$

Plane #1: C1 C14 C13 C12 C11 C2
Plane #2: C3 C4 C9 C10 C11 C2
Plane #3: C17 C18 C23 C24 C25 C16
Plane #4: C5 C6 C7 C8 C9 C4
Plane #5: C16 C25 C26 C27 C28 C15
Plane #6: C19 C20 C21 C22 C23 C18
Plane #7: C69 C74 C73 C72 C71 C70

Considering plane #1
#3@1_555 (+X,+Y,+Z)
angle: 54.504, centroid-centroid distance: 3.882, shift distance 1.765

Considering plane #2
#4@1_555 (+X,+Y,+Z)
angle: 43.605, centroid-centroid distance: 3.612, shift distance 1.326

Considering plane #3
#5@2_556 (-X,-Y,1-Z)
angle: 19.977, centroid-centroid distance: 3.999, shift distance 1.009

Considering plane #4
No interactions found

Considering plane #5
No interactions found

Symmetry codes:
1_555 +X,+Y,+Z
2_555 -X,-Y,-Z

Quantum-chemical calculations

Calculations of **2**, [**2**·F]$^-$, [**2**·Cl]$^-$, [**2**·Br]$^-$ and [**2**·I]$^-$ were performed in the Orca 5.0.3 package, unless otherwise noted. The density functional theory (DFT) with the functional PBE0[10], empirical dispersion corrections D3BJ[11] and the def2-TZVPD[12] basis set were used. The indicated variant of the def2 basis set with diffuse functions has been chosen because anion structures were calculated in this work. To overcome problems with strong linear dependencies in basis sets, the Orca option "sthresh=1e-6" has been utilized consistently in all respective cases. It should be noted that even with this setting the convergence of electronic solutions was very poor and unstable in many cases. The other Orca settings were as usual: RIJCOSX, TightSCF and DefGrid3. Geometrical optimizations of free structures were performed starting from crystal structures (whenever available) and energetically most favorable conformers found with the CREST software[13] at the GFN2-xTB semi-empirical level of theory[14]. The calculations were unstable and we utilized a special scheme consisting of several stages. First, the low DFT level, PBE-D3BJ/def2-SV(P), was used to optimize all trial structures. Of those selected most stable conformers were further optimized at the PBE0-D3BJ/def2-TZVPD level using default integration grid and convergence (SCF and geometry) settings. Finally, the most stable candidate structures were further optimized at this level of theory but using a better grid (DefGrid3) and tighter convergence criteria, TightSCF and TightOpt. The structures with lowest energies (see file CartesianXYZ.txt for coordinates) are shown in Figures S39 – S43. The harmonic frequencies and thermodynamic functions were calculated in the same way as described in our previous work[1]. The gas-phase enthalpies of formations for the adducts [**2**·F]$^-$, [**2**·Cl]$^-$, [**2**·Br]$^-$ and [**2**·I]$^-$ were calculated by using the formal scheme with the reference:

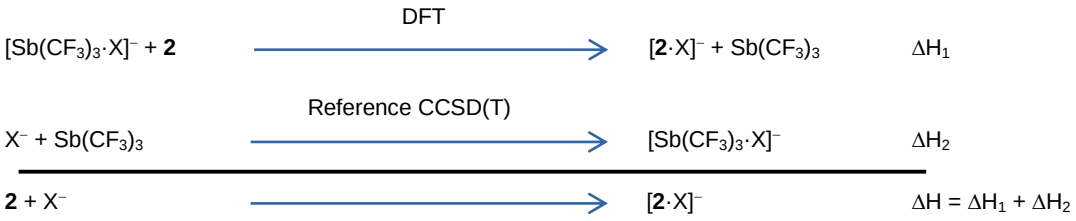

Here, X$^-$ is F$^-$, Cl$^-$, Br$^-$, I$^-$. The enthalpies ΔH_1 are calculated at the DFT level in this work and the reference enthalpies ΔH_2 were taken from our previous work.[1] They were obtained on the basis of electronic energies from ae-DLPNO-CCSD(T)/def2-QZVPPD calculations. Also on the basis of our previous calibration[1] we assume the uncertainty of our ΔH to be 2 kcal mol^{-1}. The results are summarized in Table S4. Note, that the reference system in this work was designed for consistency across all the studied compounds. However, for comparison with other investigations, we have also calculated the gas-phase fluoride ion affinity of **2** using Me_3Si–F as the reference with $-\Delta H$ = 227.7 kcal/mol (952.5 kJ/mol)[15]. The resulting value was $-\Delta H$ = 92.8 kcal/mol (388.3 kJ/mol).

For estimating the influence of the basis set superposition error (BSSE), calculations of energies have been performed for the reaction (X = F, Cl, Br and I):

[Sb(CF$_3$)$_3$·X]$^-$ + **2** → [**2**·X]$^-$ + Sb(CF$_3$)$_3$

First, reaction energies were calculated using the PBE0-D3BJ/def2-TZVP approximation, taking molecular structures optimized at this level. Next, energies were calculated for the optimized structures as before, but also taking into account the geometrical Counterpoise Corrections (gCP). For this, in Orca the option GCP(DFT/TZ) has been utilized. The results are summarized in Table S5. The average difference between the two protocols was −0.6 kcal/mol. The maximal difference was 5.9 kcal/mol for the reaction with X = Cl. Note, that in the original calculations of enthalpies (Table S4) we applied the larger def2-TZVPD basis sets containing additional diffuse functions in comparison to def2-TZVP. Thus, the actual BSSE error must be significantly smaller than the values in Table S5. The reason for using def2-TZVP in the testing calculations is that the gCP approximation was parametrized for basis sets only up to def2-TZVP. In summary, it can be concluded that BSSE does not play a significant role in our calculations.

For the optimized structures wavefunctions have been calculated at the PBE0/def2-TZVPD level using Gaussian 16 package[16] and subsequently analyzed applying quantum theory of atoms in molecules (QTAIM)[17] as implemented in the AIMAll program suite[18]. Within the same program the interacting quantum atoms (IQA) analysis[19] was performed. The results are listed in Table S6 and the respective molecular graphs with bond paths are shown in Figures S44 – S48. A similar calculation has been performed for the isolated molecule of **2** with coordinates taken from the crystal structure. For the results see Table S7.

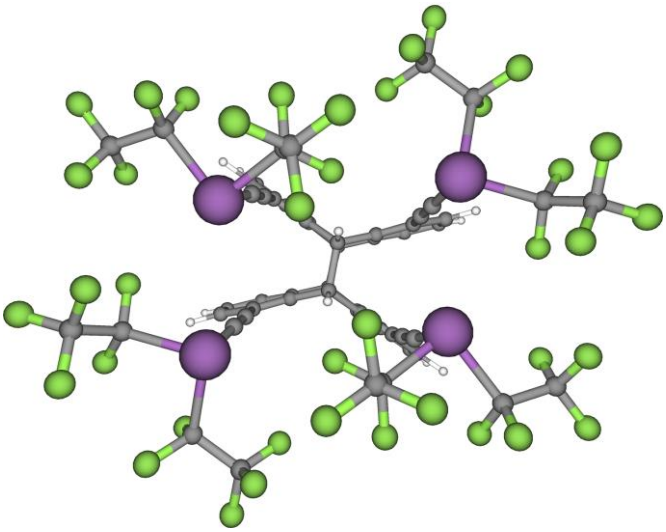

Figure S39. Optimized molecular structure of **2**.

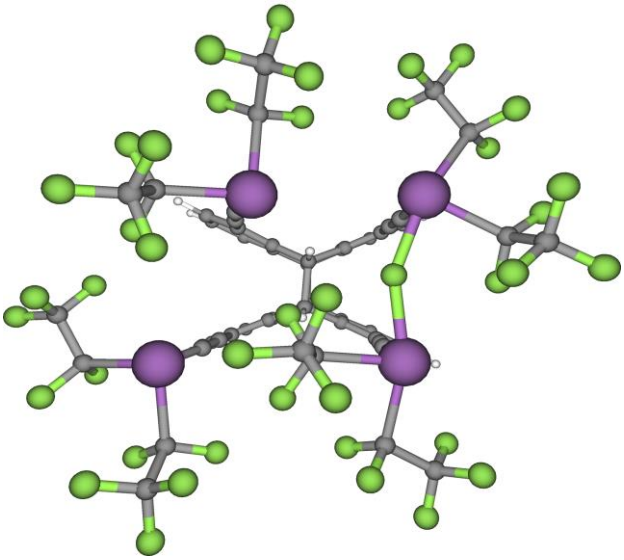

Figure S40. Optimized molecular structure of [**2**·F]$^-$.

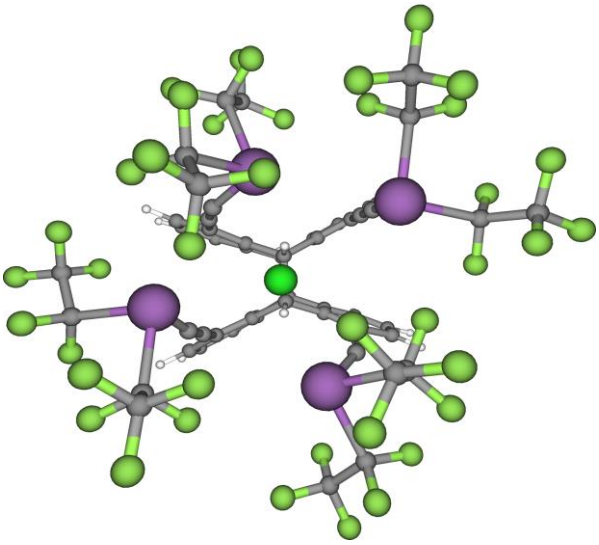

Figure S41. Optimized molecular structure of [**2**·Cl]$^-$.

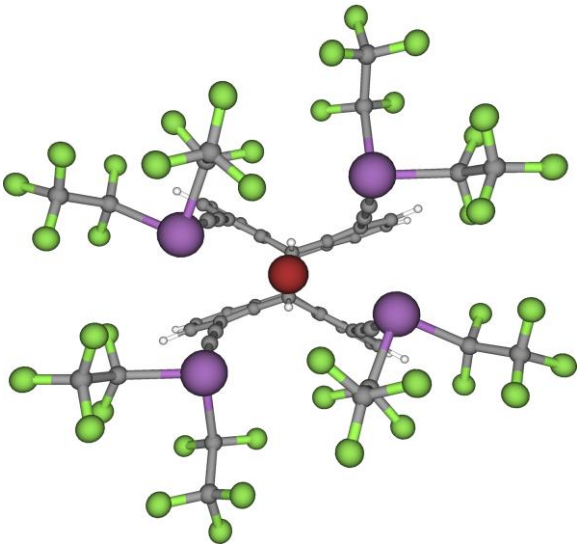

Figure S42. Optimized molecular structure of [**2**·Br]$^-$.

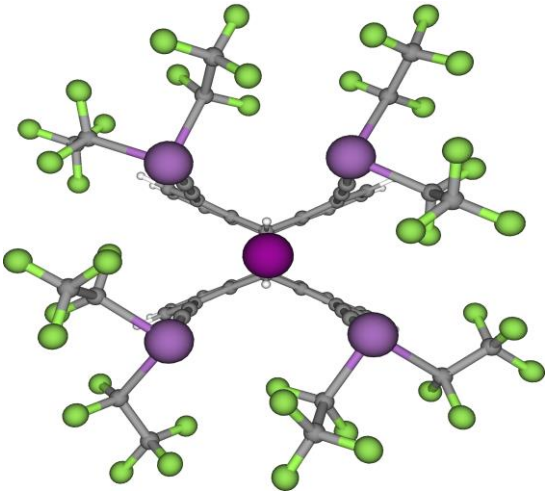

Figure S43. Optimized molecular structure of [**2**·I]$^-$.

Table S4. Enthalpies of formations for complexes of **2** with X^-.

Complex	ΔH, kcal/mol
[**2**·F]$^-$	−91.1
[**2**·Cl]$^-$	−93.2
[**2**·Br]$^-$	−95.0
[**2**·I]$^-$	−94.4

Table S5. Reaction energies taking geometrical Counterpoise Corrections (gCP) into account.

Reaction with X[a]	ΔE(DFT),[b] kcal/mol	ΔE(DFT+gCP),[c] kcal/mol	$\Delta(\Delta E)$,[d] kcal/mol
X = F	−19.8	−16.4	−3.4
X = Cl	−21.3	−27.2	5.9
X = Br	−22.9	−20.0	−2.9
X = I	−21.9	−19.9	−2.1

[a] $[Sb(CF_3)_3{\cdot}X]^-$ + **2** → [**2**·X]$^-$ + $Sb(CF_3)_3$.
[b] Calculated from energies of molecules optimized at the PBE0-D3BJ/def2-TZVP level of theory.
[c] Calculated from energies with added gCP correction.
[d] $\Delta(\Delta E) = \Delta E$(DFT) − ΔE(DFT+gCP).

Table S6. Results[a] of QTAIM and IQA analyses for selected atom pairs in **2** and [**2**·X]$^-$. All quantities are in atomic units, unless otherwise stated. Note that the atom numbering here refers to the that in Figures S44–48 and is different from the main text.

Molecule/ Pair of atoms	q(A)	q(B)	f_{AB}	ρ_{BCP}	$\nabla^2\rho_{BCP}$	E_{int}^{AB}	$V_{eeX}^{AB}/E_{int}^{AB}$, %
2							
Sb1···Sb3	1.30	1.29	0.08	0.009	0.014	0.174	7
Sb2···Sb4	1.29	1.29	0.08	0.009	0.014	0.173	7
[**2**·F]$^-$							
Sb1···F113	1.49	–0.81	0.33	0.054	0.171	–0.366	19
Sb2···F113	1.33	–0.81	0.0000_8	-	-	–0.088	0
Sb3···F113	1.44	–0.81	0.35	0.056	0.183	–0.368	20
Sb4···F113	1.34	–0.81	0.01	-	-	–0.125	2
Sb3···Sb4	1.44	1.34	0.05	0.006	0.010	0.196	4
[**2**·Cl]$^-$							
Sb1···Cl113	1.38	–0.73	0.26	0.026	0.049	–0.211	21
Sb2···Cl113	1.38	–0.73	0.19	0.019	0.039	–0.188	16
Sb3···Cl113	1.35	–0.73	0.09	0.010	0.024	–0.148	9
Sb4···Cl113	1.37	–0.73	0.27	0.028	0.050	–0.218	21
[**2**·Br]$^-$							
Sb1···Br113	1.34	–0.69	0.28	0.026	0.039	–0.193	24
Sb2···Br113	1.34	–0.69	0.13	0.013	0.026	–0.148	13
Sb3···Br113	1.35	–0.69	0.13	0.013	0.026	–0.148	13
Sb4···Br113	1.34	–0.69	0.28	0.026	0.039	–0.193	24
[**2**·I]$^-$							
Sb2···I1	1.34	–0.64	0.25	0.018	0.027	–0.157	23
Sb3···I1	1.34	–0.64	0.23	0.017	0.026	–0.152	22
Sb4···I1	1.33	–0.64	0.24	0.017	0.025	–0.151	22
Sb5···I1	1.35	–0.64	0.18	0.013	0.021	–0.138	18

[a] q – atomic charge; f_{AB} – electron delocalization index; ρ_{BCP} – electron density at the bond critical point; $\nabla^2\rho_{BCP}$ – Laplacian of the electron density at the bond critical point; E_{int}^{AB} – total interaction energy between atoms A and B in IQA analysis; $V_{eeX}^{AB}/E_{int}^{AB}$ – electron exchange-correlation contribution in E_{int}^{AB} in percent, negative values indicate different signs of V_{eeX}^{AB} and E_{int}^{AB}.

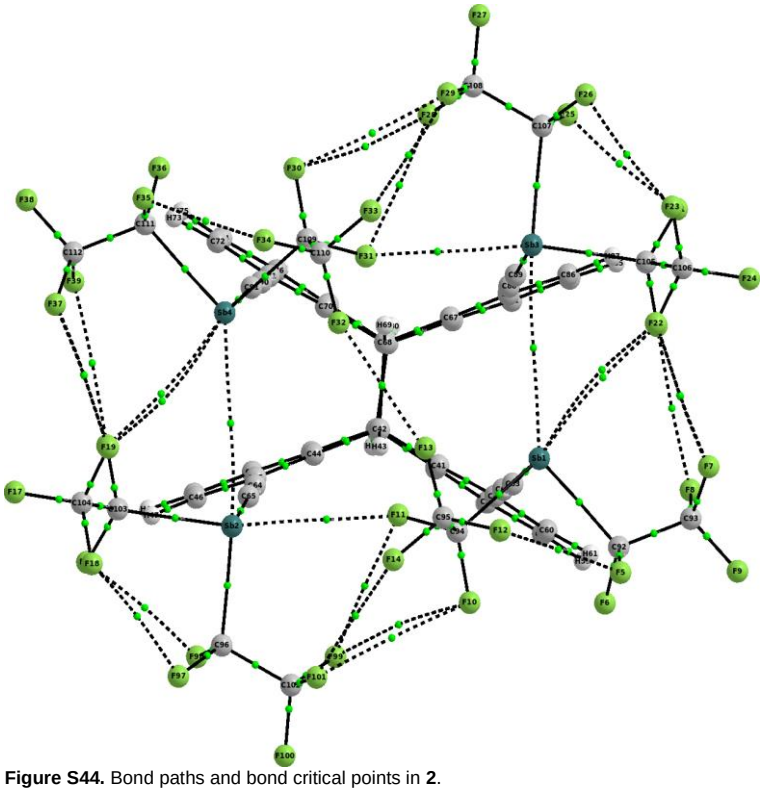

Figure S44. Bond paths and bond critical points in **2**.

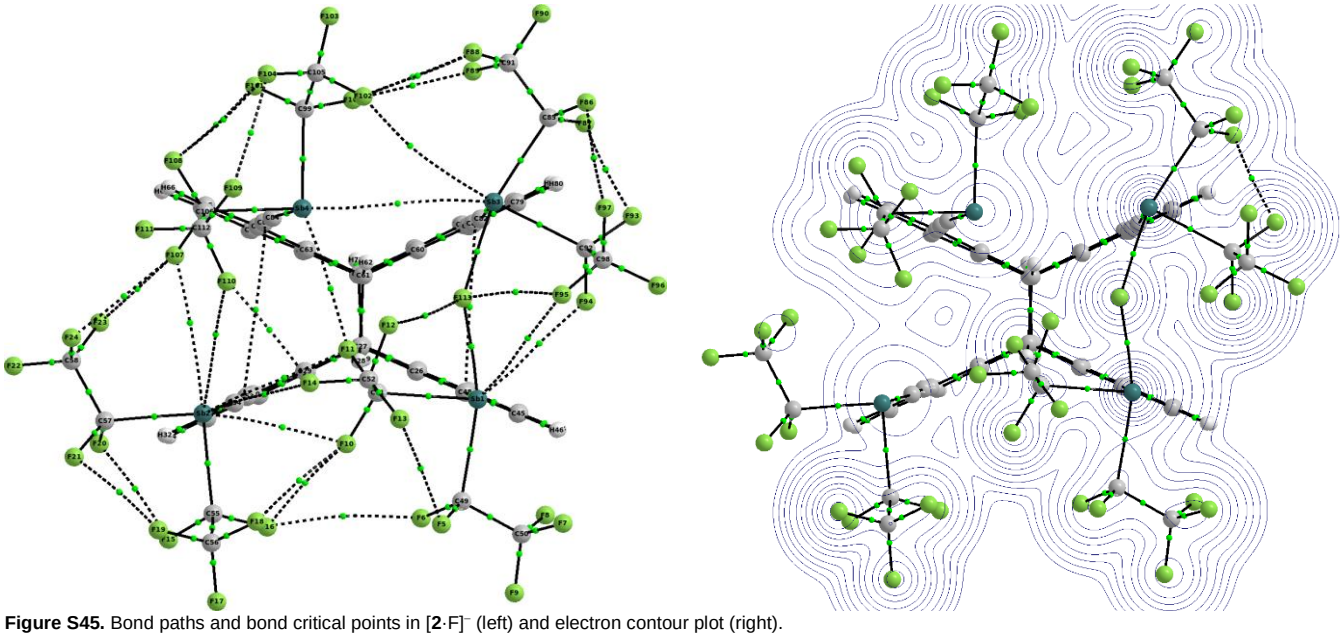

Figure S45. Bond paths and bond critical points in [**2**·F]$^-$ (left) and electron contour plot (right).

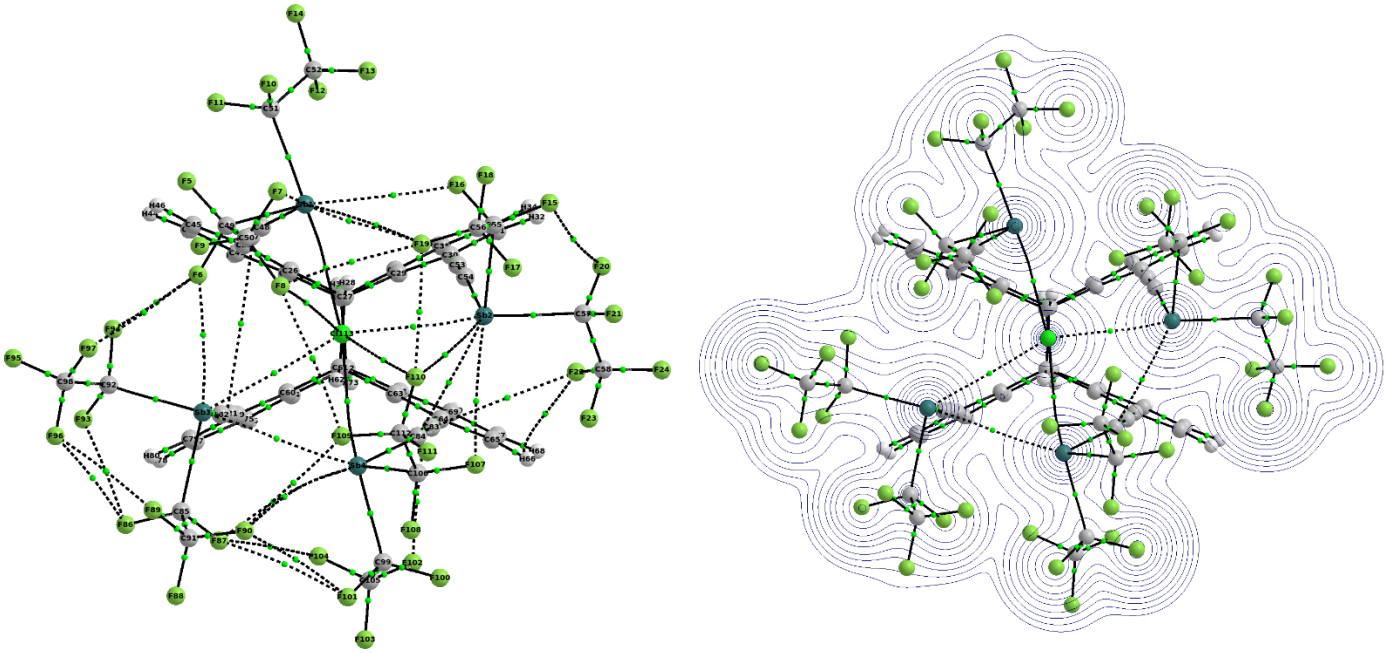

Figure S46. Bond paths and bond critical points in [**2**·Cl]$^{-}$ (left) and electron contour plot (right).

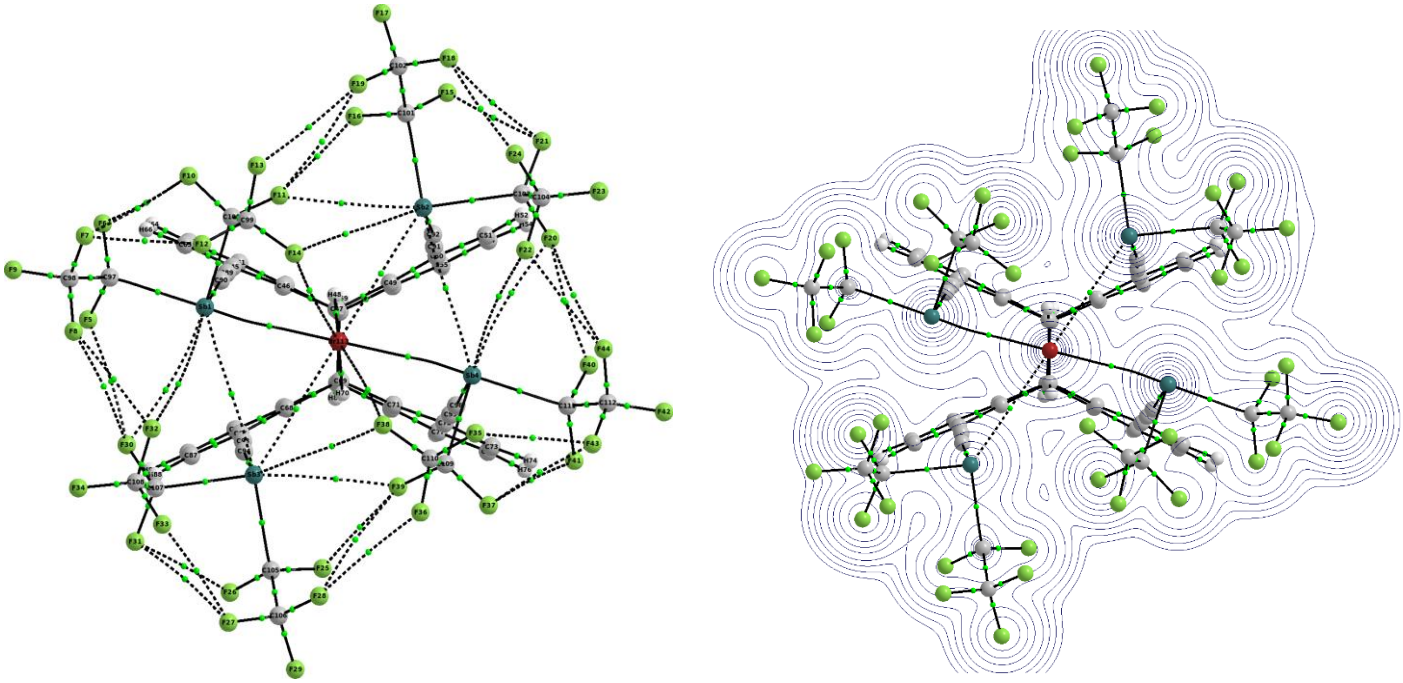

Figure S47. Bond paths and bond critical points in [**2**·Br]$^{-}$ (left) and electron contour plot (right).

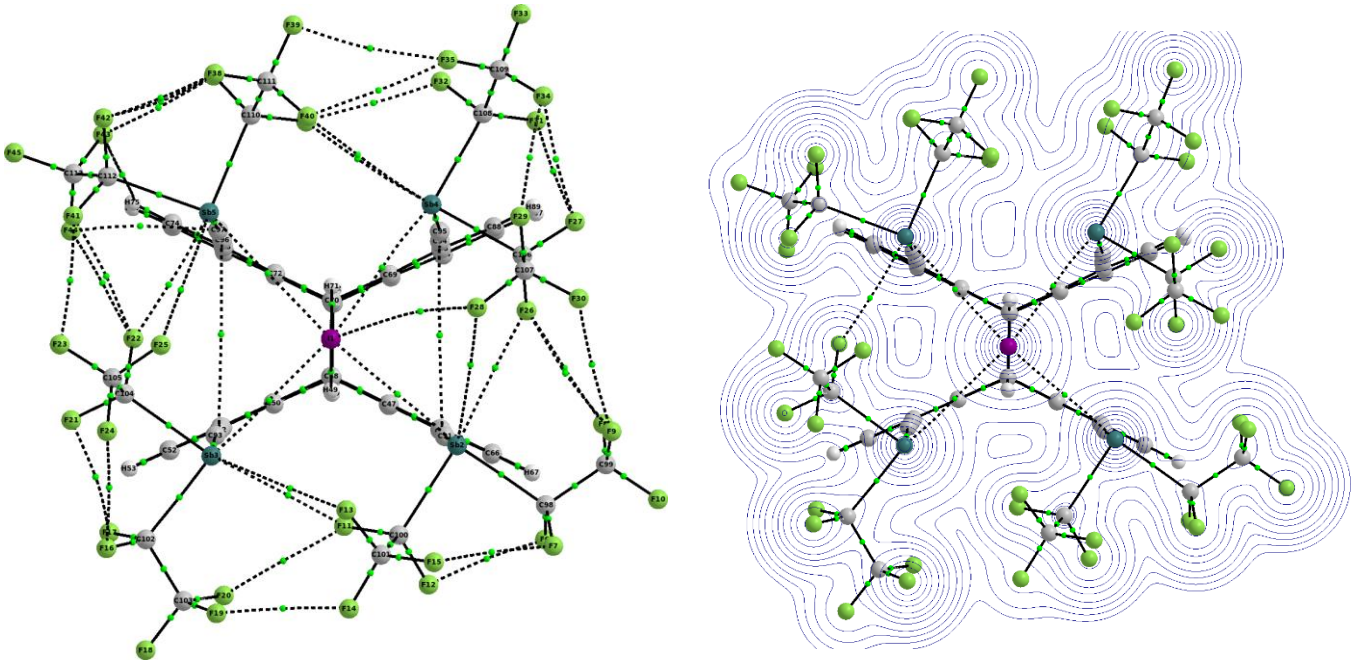

Figure S48. Bond paths and bond critical points in [**2**·I]$^-$ (left) and electron contour plot (right).

Table S7. Interaction energies E_{int}^{AB} (in atomic units) and distances (in Å) between atoms of selected atom pairs as obtained from IQA analysis for the structure of **2** in the crystal phase. The angle α is the largest angle found for the respective fragment C–Sb···F. For atom numbering see Figure S49.

Atom pair	E_{int}^{AB}	r^c [Å]	α^d [°]
(Sb3···F25)[a]	–1.93×10^{-1}	2.896	121.9
(Sb2···F19)[a]	–1.57×10^{-1}	3.290	135.8
(Sb2···F108)[b]	–1.52×10^{-1}	3.044	170.6
(Sb4···F111)[a]	–1.49×10^{-1}	3.255	125.6
(Sb3···F29)[a]	–1.48×10^{-1}	3.269	131.5
(Sb4···F110)[a]	–1.47×10^{-1}	3.382	134.8
(Sb1···F25)[b]	–1.37×10^{-1}	3.223	168.8
(Sb3···F35)[b]	–1.36×10^{-1}	3.220	166.0
(Sb2···F11)[b]	–1.34×10^{-1}	3.255	162.8
(Sb3···F107)[b]	–1.22×10^{-1}	3.311	145.5
(Sb4···F20)[b]	–1.11×10^{-1}	3.855	163.5

[a] Contacts within one $Sb(C_2F_5)_2$ group.
[b] Contacts between two $Sb(C_2F_5)_2$ groups.
[c] Distance between atoms.
[d] Largest angle in fragments C–Sb···F.

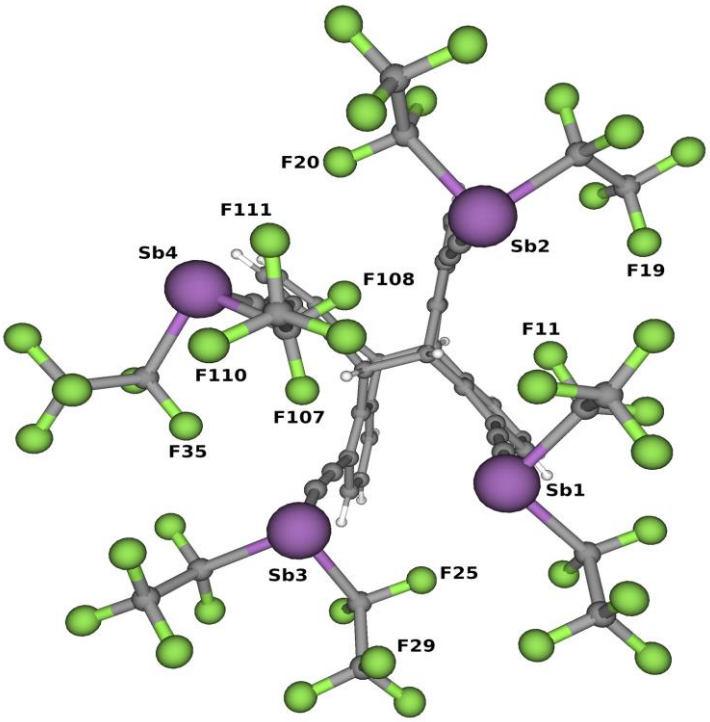

Figure S49. Structure of **2** in the crystalline state with the numeration used in calculations of Table S7.

References

[1] J. L. Beckmann, J. Krieft, Y. V. Vishnevskiy, B. Neumann, H.-G. Stammler and N. W. Mitzel, *Angew. Chem.* (accepted), https://doi.org/10.1002/anie.202310439

[2] P. Niermeier, K. A. M. Maibom, J.-H. Lamm, B. Neumann, H.-G. Stammler and N. W. Mitzel, *Chem. Sci.*, 2021, **12**, 7943.

[3] M. J. Hynes, *J. Chem. Soc., Dalton trans.*, 1993, 311–312.

[4] O. V. Dolomanov, L. J. Bourhis, R. J. Gildea, J. A. K. Howard and H. Puschmann, *J. Appl. Crystallogr.*, 2009, **42**, 339.

[5] G. M. Sheldrick, *Acta Crystallogr. A*, 2015, **71**, 3.

[6] G. M. Sheldrick, *Acta Crystallogr. C*, 2015, **71**, 3.

[7] A. Bondi, *J. Phys. Chem.*, 1964, **68**.

[8] M. Mantina, A. C. Chamberlin, R. Valero, C. J. Cramer and D. G. Truhlar, *J. Phys. Chem. A*, 2009, **113**, 5806.

[9] P. Pyykkö, M. Atsumi, *Chem. Eur. J.*, 2009, **15**, 186.

[10] C. Adamo and V. Barone, *J. Chem. Phys.*, 1999, **110**, 6158–6170.

[11] S. Grimme, S. Ehrlich and L. Goerigk, *J. Comput. Chem.*, 2011, **32**, 1456–1465.

[12] D. Rappoport and F. Furche, *J. Chem. Phys.*, 2010, **133**, 134105.

[13] P. Pracht, F. Bohle and S. Grimme, *Phys. Chem. Chem. Phys.*, 2020, **22**, 7169–7192.

[14] C. Bannwarth, S. Ehlert and S. Grimme, *J. Chem. Theory Comput.*, 2019, **15**, 1652–1671.

[15] P. Erdmann, J. Leitner, J. Schwarz, L. Greb, *ChemPhysChem*, 2020, **21**, 987–994.

[16] M. J. Frisch, G. W. Trucks, H. B. Schlegel, G. E. Scuseria, M. A. Robb, J. R. Cheeseman, G. Scalmani, V. Barone, G. A. Petersson, H. Nakatsuji, X. Li, M. Caricato, A. V. Marenich, J. Bloino, B. G. Janesko, R. Gomperts, B. Mennucci, H. P. Hratchian, J. V. Ortiz, A. F. Izmaylov, J. L. Sonnenberg, D. Williams-Young, F. Ding, F. Lipparini, F. Egidi, J. Goings, B. Peng, A. Petrone, T. Henderson, D. Ranasinghe, V. G. Zakrzewski, J. Gao, N. Rega, G. Zheng, W. Liang, M. Hada, M. Ehara, K. Toyota, R. Fukuda, J. Hasegawa, M. Ishida, T. Nakajima, Y. Honda, O. Kitao, H. Nakai, T. Vreven, K. Throssell, J. A. Montgomery Jr., J. E. Peralta, F. Ogliaro, M. J. Bearpark, J. J. Heyd, E. N. Brothers, K. N. Kudin, V. N. Staroverov, T. A. Keith, R. Kobayashi, J. Normand, K. Raghavachari, A. P. Rendell, J. C. Burant, S. S. Iyengar, J. Tomasi, M. Cossi, J. M. Millam, M. Klene, C. Adamo, R. Cammi, J. W. Ochterski, R. L. Martin, K. Morokuma, O. Farkas, J. B. Foresman and D. J. Fox, *Gaussian 16 Revision C.01*, Gaussian Inc. Wallingford CT, 2016.

[17] R. F. W. Bader, *Atoms in Molecules - A Quantum Theory*, Oxford University Press, Oxford, 1990.

[18] K. A. Todd, *AIMAll Version 19.10.12, TK Gristmill Software*, aim.tkgristmill.com, 2019.

[19] M. A. Blanco, A. Martín Pendás and E. Francisco, *J. Chem. Theory Comput.*, 2005, **1**, 1096–1109.